

Petrogenesis and tectonic implications of Late Triassic granitoids in the Alananshan, East Kunlun belt: evidence from geochemistry, geochronology, and zircon Hf isotopic compositions

Zhen Xi¹ · Huan Li²  · Safiyanu Muhammad Elatikpo^{2,3} · Guangming Gao² · Decheng Ma⁴

Received: 6 April 2022 / Revised: 23 July 2022 / Accepted: 27 July 2022 / Published online: 6 September 2022
© The Author(s), under exclusive licence to Science Press and Institute of Geochemistry, CAS and Springer-Verlag GmbH Germany, part of Springer Nature 2022

Abstract The Qimantag in the East Kunlun Orogenic Belt has widespread Triassic magmatic rocks that have received scant attention, with an unresolved issue relating to its petrogenesis and geodynamics. In this paper, we used zircon U-Pb–Hf isotopes and whole-rock geochemistry to trace the petrogenesis and tectonic settings of the moyite and monzogranite from the Qimantag Alananshan, East Kunlun. The moyite and monzogranite are silicic ($\text{SiO}_2 \sim 69.9\text{--}76.41\%$), highly alkali ($\text{Na}_2\text{O} + \text{K}_2\text{O} \sim 7.29\text{--}8.96\text{ wt.\%}$), with $\text{Mg}^{\#}$ about 10.4–30.34, indicative of a high-K calc-alkaline rock series. The rare earth element patterns diagram is right-leaning, with a negative Eu anomaly ($\delta\text{Eu} = 0.31\text{--}0.68$). They are enriched in Rb, K, and light rare earth elements but depleted in Nb, Ta, and Ti, with abundant amphibole, typical of I-type granites. U–Pb on zircon constrained the emplacement of the moyite at $223.9 \pm 2.6\text{ Ma}$ and monzogranite at $226.9 \pm 2.9\text{ Ma}$. The $\epsilon\text{Hf}(t)$ values range from -2.8 to $+0.1$ except for one outlier value of -7.0 , corresponding two-stage model age of $1249\text{--}1437\text{ Ma}$. Our combined geochemical and isotopic results indicate that the moyite and monzogranite were derived from partial melting of the lower thicken-

crust with the contribution from the older basement materials. These rocks formed in a post-collision setting that is transitional between compressive collision and extension orogeny.

Keywords I-type granite · Petrogeochemistry · Triassic magmatic rocks · Hf isotope · East Kunlun orogenic belt

1 Introduction

The East Kunlun Orogenic Belt (EKOB), a part of the central orogenic belt, is located at the Qaidam and Qiangtang blocks in the northern end of the Qinghai-Tibet Plateau. It is a composite orogenic belt that has experienced multiple cycles of collision tectonics (Mo et al. 2007). The Qimantag area, a part of the EKOB, is adjacent to the Qaidam Basin, bounded by the Altun Paleozoic orogenic belt to the west and the Middle Kunlun micro-continent and the Kumukuri Basin to the south. Its geological characteristics are a microcosm of the tectonic–magmatic evolution of East Tethys. Reconstructing the tectonic–magmatic evolution in this area not only helps to understand the formation history of the EKOB but also is of great significance for an in-depth understanding of the evolution of the northern Qinghai-Tibet Plateau.

During the Early Paleozoic, the Pro-Tethys Qimantag oceanic crust subducted under the Qaidam; subsequent collision, delamination, and slab breakoff resulted in granite magmatism (Meng et al. 2013; Li et al. 2018a, b, 2020; Dong et al. 2020). Qimantag area preserves the tectono-magmatic products from pre-Proterozoic to Late-Mesozoic Era. Several kinds of research (e.g., Chen et al. 2015; Dong et al. 2018; Zhao et al. 2019; Zheng et al.

✉ Huan Li
lihuan@csu.edu.cn

¹ School of Municipal and Geomatics Engineering, Hunan City University, Yiyang 413000, China

² School of Geosciences and Info-Physics, Central South University, Changsha 410083, China

³ Department of Geology, Ahmadu Bello University, Zaria, Nigeria

⁴ No. 701 Geological Team, Xinjiang Nonferrous Geexploration Bureau, Changji 831100, China

2018), including geochemical, geochronological, and isotope geochemistry, have been carried out on the magmatism and mineralization potential of the Qimantag area. However, there are still many disputes on the igneous magma source or tectonic setting, even the precise age of one same intrusion (Shi et al. 2017; Bai et al. 2016; Gao et al. 2012, 2014; Yao et al. 2018). As an example, the petrogenetic model of Triassic I-type granitoids in Qimantag is open to debate with its magma source linked to enriched mantle, juvenile crust or ancient material of lower crust (Xiong et al. 2016; Yin et al. 2017; Zhou et al. 2020). At different locations in the Qimantag orogenic belt, the source of igneous magma and the precise age of the evolutionary dynamics of the orogenic belt are still controversial (Shi et al. 2017; Bai et al. 2016; Gao et al. 2012; 2014; Yao et al. 2018).

The Xinjiang region in the western part of the Qimantag experienced late tectonic movement, with relatively scattered Triassic magmatic rocks which have received scant attention. Some research conclusions are also controversial, such as the dynamic process of the orogenic belt. Zhou et al. (2015) suggested that the Weibao granodiorite in the west of Qimantag in the Late Triassic was formed in the post-collisional stage of the lower crust-mantle contamination, while Xia et al. (2017) believed that the early Triassic Dalaku ultrabasic pluton at the western end of Qimantag was formed in the post-collision extension stage. The magma source is the enriched lithosphere mantle. The diversity and complexity of the Triassic magmatic rocks' genesis and tectonic setting, and their dynamic mechanisms are worthy of further study and discussion.

Alananshan is located in the middle of Qimantag, EKOB, adjacent to the Adatan fault. It is the hub connecting the Qimantag orogenic belt to the Central Kunlun microcontinent and the east and west parts of the Qimantag. The present contribution integrated petrology, zircon U-Pb-Hf isotope systematics and shed light on the petrogenesis and geodynamic evolution of the EKOB.

2 Regional geology and petrography

The EKOB runs from the Early Paleozoic Apa-Mangya junction zone (Altun-southern margin fault zone) in the north and is bounded by the Quyuhu-Muztag Late Paleozoic ophiolitic tectonic mélange zone in the south (Fig. 1) (Jiang et al. 1992). It is adjacent to the Altun orogenic belt, the West Kunlun orogenic belt and the Bayan Hala-Qiangtang block. The EKOB is divided into Qimantag Early Paleozoic tectonic mélange belt (North Qimantag terrane), Middle Kunlun microcontinental block (South Qimantag terrane), Kunzhong tectonic mélange belt and Kunnan Early Paleozoic accretionary wedge and other

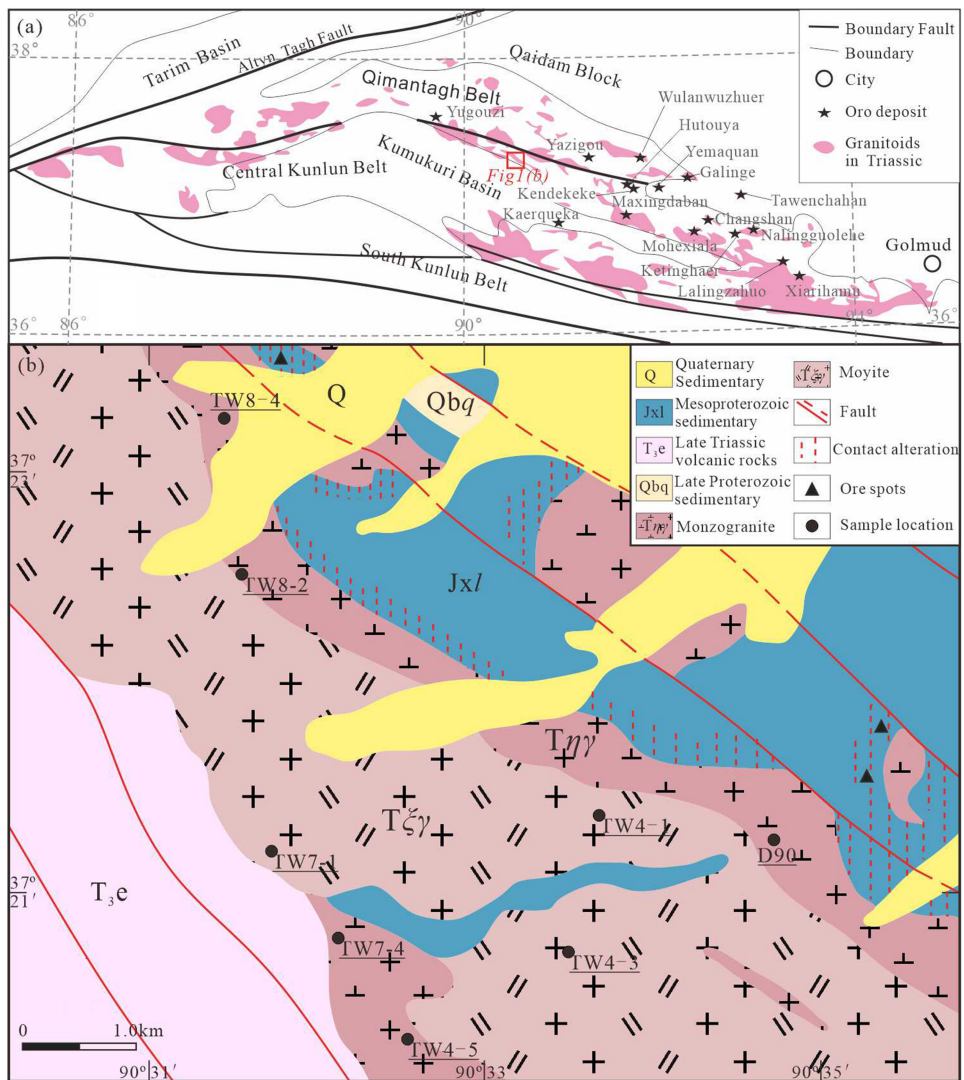
units (Fig. 1a) (Wang et al. 2009a; Yu et al. 2017). The magmatic rocks in the Qimantag terrane are mainly Ordovician-Devonian in age. In contrast, the Late Paleozoic–Mesozoic magmatic rocks are only developed in the Middle Kunlun microcontinent, during the Triassic period. Early Proterozoic metamorphic rocks, middle to late Proterozoic carbonate rocks, and clastic rocks are also exposed in the area and flysch strata of the Qimantag Group. Structural trends are dominantly northwest, e.g., the active Adatan fault, about 15 km away from Alananshan, with minor WNW and east to west trending small-scale faults in adjacent terranes.

Alananshan is located between Xinjiang and Qinghai, close to the Adatan thrust fault zone (Fig. 1). The Alananshan pluton is a major lithology amidst minor other rocks in the surrounding areas. The Alananshan pluton trends NW with an approximated area of 26 km² with a width between 1.5 and 3.5 km. The middle of this pluton is a brown coarse-grained to porphyritic moyite representing the central pluton and accounted for about two-thirds of the pluton area coverage. Flanked at the north and south of the Alananshan pluton are coarse-grained to porphyritic monzogranite and medium-coarse-grained monzogranite, respectively, accounting for about one-third of the pluton's size. A contact relationship can be seen between these intrusive rocks and volcanic rock of the Upper Triassic Erlashan Formation (T₃e) at the southern part of the pluton. On the north side, the contact relationship between the Alananshan pluton and the Jixian Langyashan carbonate Formation (JxI) is marked by a fault. Xenolith of surrounding country-rock is also present in the Alananshan pluton, mainly at the edges. Skarn zones are often developed in the intrusion's contact zone, with the occurrence of iron mineralization and copper-lead-zinc-tungsten polymetallic mineralizations. Drilling exploration is currently underway, and it is hoping to find medium-sized and above skarn-type copper polymetallic deposits (Fig. 1b).

The contact relationship between the moyite and the monzogranite is sharp and pronounced (Fig. 2a). Minor late-stage aplite dikes cross-cut parts of the monzogranite, mainly around the edge of the pluton.

Three moyites (samples TW4-1, TW4-3 and TW7-1) and five monzogranites (samples TW8-4, TW4-5, TW7-4, TW8-2 and D90) were collected from Alananshan pluton. The sampling locations are shown in Fig. 1b. The moyite is red coarse-grained and sometimes porphyritic in texture. They are also often grey and massive. Megascopic examination of hand specimen reveals K-feldspar and plagioclase megacrysts in a matrix dominated by feldspars and quartz (Fig. 2b, c). K-feldspar is semi-idiomorphic granular with argillization, and minor small plagioclase crystals are contained in some K-feldspar phenocrysts. Plagioclase

Fig. 1 **a** Tectonic sketch map of the Qimantag (modified after Jiang et al. 1992; Dong et al. 2018); **b** Geological sketch map of Alananshan



shows a slight degree of sericitization, indicating alteration. Biotite is also present but minor.

Compared to the moyite, the monzogranite is relatively light red to greyish with a medium-coarse-grained texture. It is composed of plagioclase (20–30 %), K-feldspar (30–40 %), and quartz (20–30 %). Others are the biotite flakes and amphibole grains with minor opaque minerals (Fig. 2d, e). The twin planes of plagioclase appear cloudy and altered, indicative of sericitization. Quartz is the dominant matrix in the monzogranite sample.

3 Analytical methods

3.1 Major and trace elements

Three moyites (samples TW4-1, TW4-3 and TW7-1) and five monzogranites (samples TW8-4, TW4-5, TW7-4,

TW8-2 and D90) were pulverized to 200 mesh size (powder form), fused in a lithium-borate flux with lithium nitrate as an oxidizing agent, and poured into a platinum mould to generate a fused disk for X-Ray Fluorescence Analysis. The major element concentrations and Loss-on-ignition (LOI, at 1000 °C) were measured for each sample. The XRF was operated at 50 kV (voltage) using a current of 50 mA. In addition, we undertook a chemical analysis to determine ferrous oxide content. Both analyses were done at the Institute of Geology for Nuclear Industry, Beijing, China.

Trace elements were analyzed by a Finnigan MAT high-resolution inductively coupled plasma mass spectrometry (HR-ICP-MS, Element I. The powder sample was added to a lithium metaborate/lithium tetraborate flux, mixed and fused in a furnace at 1025 °C. After it cooled (melt), it was dissolved in an acid mixture composed of nitric, hydrochloric and hydrofluoric acids. The resultant solution

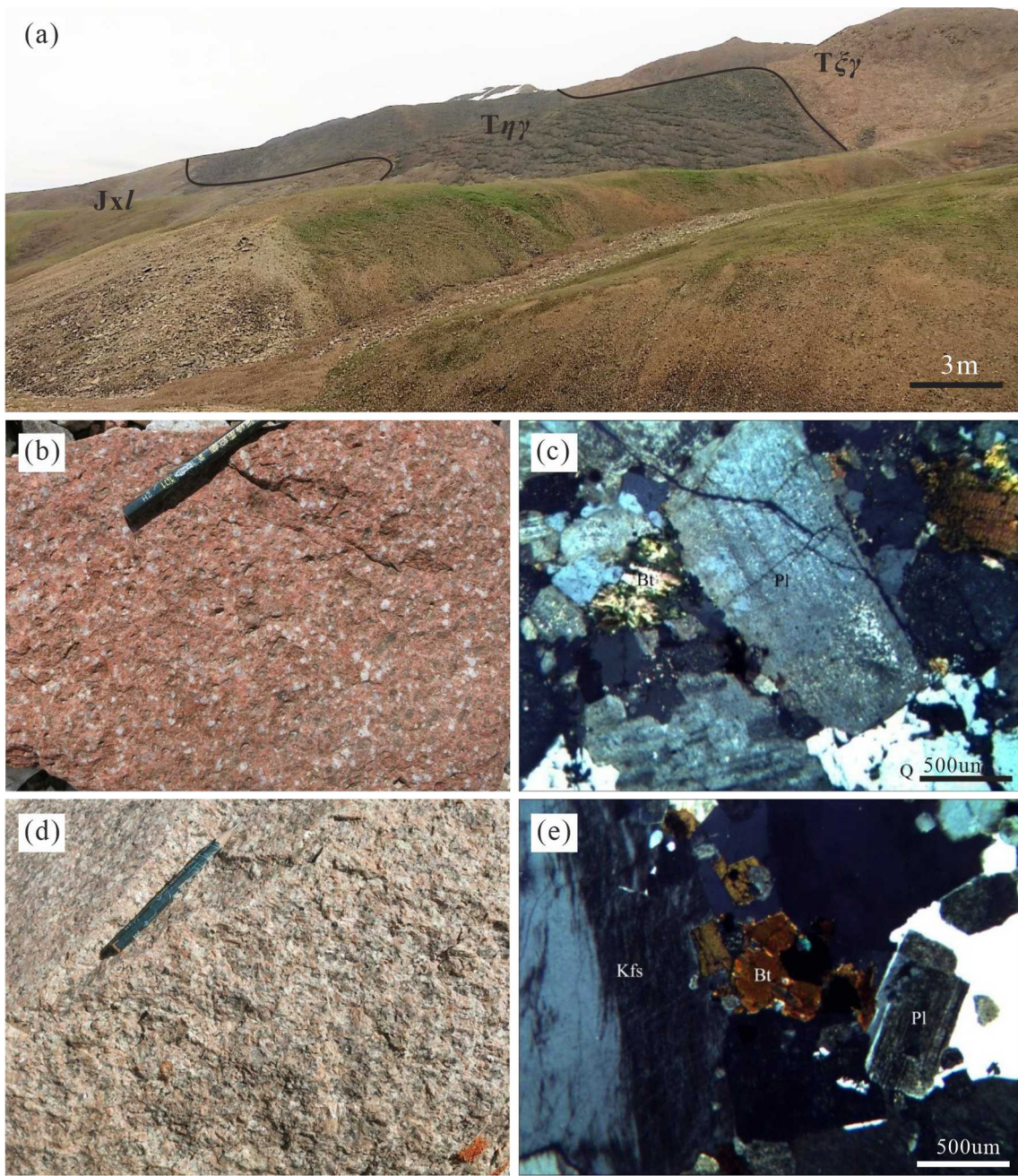


Fig. 2 Field and photomicrographs of the moyite and monzogranite in the Alananshan. **a** surface exposure of the moyite and monzogranite intruding the country rock; **b, c** moyite sample and **c, d** monzogranite sample. Kfs, K-feldspar; Bt, biotite; Pl, plagioclase

was analyzed by ICP-MS. Trace element content greater than 10 ppm has a relative error of less than 5%, while those with less than 10 ppm have less than 10 %.

3.2 Zircon U–Pb age and Hf isotope compositions

Fresh samples of moyite (TW4-3) and monzogranite (TW8-4) were crushed, and zircons were separated. Both reflected, transmitted, and cathodoluminescence (CL) images were obtained at the Experimental Test Center of

Xinjiang Institute of Ecology and Geography, Chinese Academy of Sciences. The combined study of these images guided our choice of laser ablation spot selection, and areas without visible fracture and inclusions were chosen for the U–Pb isotopes analysis.

Zircon U–Pb dating analyses were performed by LA-ICP-MS at the Xinjiang Institute of Ecology and Geography, Chinese Academy of Sciences, China. Laser sampling was conducted using a NewWave Research NWR 193 nm ArF excimer laser. An Agilent 8800 ICP-MS instrument

was used to acquire ion-signal intensities. Helium was applied as a carrier gas. Argon was used as the make-up gas and mixed with the carrier gas via a T-connector before entering the ICP. The laser beam spot used in the analysis has a diameter of 32 μm . Zircon 91,500 was used as an external standard, and the standard zircon GJ-1 as a blind sample to test the quality of U–Pb dating data. The obtained analytical results of standard samples (Electronic Supplementary Material) yielded: (1) zircon 91,500, a Concordia age = 1062.78 ± 6.26 Ma (MSWD = 0.25; n = 14) and, (2) GJ-1, a weighted mean age 598.48 ± 9.49 Ma (MSWD = 0.21; n = 3), which are consistent with the recommended values for these standards within error (1064 ± 4 Ma for 91,500, Woodhead and Herdt 2005; 604 ± 4 Ma for GJ-1, Jackson et al. 2004). Detailed operating conditions for the instrument and analytical procedures were described in Zong et al. (2017). Isoplot/Ex,3 was used to calculate the weighted mean ages and plot Concordia diagrams (Ludwig 2003).

Zircon Hf isotopic analyses were performed using laser ablation-multiple collector-inductively coupled plasma mass spectrometry (LA-MC-ICP-MS) at the State Key Laboratory of Isotope Geochemistry, Guangzhou Institute of Geochemistry, Chinese Academy of Sciences. The LA-MC-CPMS consists of a Cetac Analyte HE laser ablation system coupled with a ThermoFisher Neptune Plus MC-ICPMS. We used a laser beam diameter of 50 μm with laser energy density and repetition rate at ~ 3.0 J/cm² and 8 Hz, respectively. Helium was used as the carrier gas within the ablation cell and mixed with Ar (make-up gas). Each analysis consisted of 20 s of background signal acquisition, followed by 50 s of ablation signal acquisition. During the investigation, zircon standards Plešovice, Penglai, and Qinghu (external and secondary standards) were analyzed with our samples to ensure the reliability of the analysis. The $^{179}\text{Hf}/^{177}\text{Hf}$ and $^{173}\text{Yb}/^{171}\text{Yb}$ ratios were used for calculating the mass bias of Hf (βHf) and Yb (βYb). Using an exponential correction method, the $^{179}\text{Hf}/^{177}\text{Hf}$ and $^{173}\text{Yb}/^{171}\text{Yb}$ ratios were normalized to 0.7325 for $^{179}\text{Hf}/^{177}\text{Hf}$ and 1.1248 for $^{173}\text{Yb}/^{171}\text{Yb}$ (Blichert-Toft et al. 1997). To minimize the interference of ^{176}Yb on ^{176}Hf , we measured the interference-free ^{173}Yb isotope and used $^{176}\text{Yb}/^{173}\text{Yb} = 0.7876$ (McCulloch et al. 1977) to calculate $^{176}\text{Yb}/^{177}\text{Hf}$. Additionally, for the minor interference of ^{176}Lu on ^{176}Hf , we determined the relative intensity of the interference-free ^{175}Lu isotope and used $^{176}\text{Lu}/^{175}\text{Lu} = 0.02656$ (Blichert-Toft et al. 1997) to calculate $^{176}\text{Lu}/^{177}\text{Hf}$. The mass bias of Yb (βYb) was used to calculate the mass fractionation of Lu because of their similar properties. We used an excel based software to calculate eHf(o), eHf(t), and the TDM using zircon Lu/Hf, Yb/Hf, and Hf/Hf ratios (analytical results) and crystallization ages of the rock samples. The following parameters

are included in the excel-based software we used: ^{176}Lu decay constant of 1.867×10^{-11} (Söderlund et al. 2004), chondritic ratios ($^{176}\text{Hf}/^{177}\text{Hf} = 0.282772$ and $^{176}\text{Lu}/^{177}\text{Hf} = 0.0332$; Blichert-Toft et al. 1997). Other parameters used were mean $^{176}\text{Lu}/^{177}\text{Hf}$ value = 0.015 for average continental crust, fcc = -0.548, and f_{DM} = 0.16 (GERM 2001), $^{176}\text{Lu}/^{179}\text{Hf}_{\text{DM}} = 0.0384$ and $^{176}\text{Hf}/^{179}\text{Hf}_{\text{DM}} = 0.28325$ (Nowell et al. 1998; Griffin et al. 2000). To guarantee the reliability of data acquisition, zircon standards Plešovice, Penglai, and Qinghu were analyzed with our samples, yielding $^{176}\text{Hf}/^{177}\text{Hf}$ values of 0.282478 ± 0.000017 , 0.282910 ± 0.000019 , and 0.282999 ± 0.000021 , respectively. These ratios are in agreement with the recommended values of these three standards: 0.282906 ± 0.000016 (Penglai), 0.282482 ± 0.000013 (Plešovice), and 0.282996 ± 0.000044 (Qinghu) (Sláma et al. 2008; Li et al. 2010, 2013). The major and trace element compositions, zircon U–Pb, and Hf isotopic data are presented in Tables 1, 2, and 3, respectively.

4 Results

4.1 Whole rock geochemistry

Results of whole-rock major and trace elements are listed in Table 1. Silica contents of the moyite and monzogranite samples range from 69.9 to 76.4 wt.% (Fig. 3a). They are rich in alkalis ($\text{Na}_2\text{O} + \text{K}_2\text{O} \sim 7.29$ to 8.96 wt.%), with $\text{K}_2\text{O}/\text{Na}_2\text{O}$ from 0.5 to 1.2 but dominantly less than 1. The Al_2O_3 contents of these rocks are from 12.0 to 13.8 wt.% with alumina saturation index (A/CNK) between 0.94 and 1.16, indicating their metaluminous nature (Fig. 3b). Moyite samples plot mainly into the alkali-calcic field, while monzogranite samples range from calc-alkalic to alkali-calcic (Fig. 3c, d). The measured $\text{Fe}^{3+}/\text{Fe}^{2+}$ values range from 0.01 to 0.35, indicating the reducing environment of melt crystallization.

Most trace elements in the moyite and monzogranites show compatible behavior and similar enrichment in Rb, Th, K and depleted in Ba, Nb, Ta, P, and Ti (Fig. 4b). Their $(\text{Rb}/\text{Yb})_{\text{N}}$ ratio of 9.61–275.43 (average 69.30) corroborate their enrichment in incompatible elements. The Nb-Ta depletion justifies the lower $2\text{Nb}_{\text{N}}/(\text{K} + \text{La})_{\text{N}}$ ratio of 0.08–0.27 (average 0.15), reflecting the Nb deficiency and characteristics of a subduction-related magma source. The depletion of Ta, Nb, and Hf may indicate separation and crystallization of apatite and ilmenite and is most likely indicative of calc-alkaline magmatic rocks of island arc or active continental margin affinity (Guo et al. 2018). Such an Nb-Ta and sometimes Ti depletion have also been attributed to their retention on subducting slab components during mantle lithosphere melting (Santosh et al. 2017;

Table 1 Major oxides (wt.%) and trace elements (ppm) concentration of moyites and monzogranites from the Alanansha, EKOB

Sample	Moyite			Monzogranite				
	TW4-1	TW4-3	TW7-1	TW8-4	TW4-5	TW7-4	TW8-2	D90
SiO ₂	71.15	69.9	71.45	76.41	70.73	71.25	72.85	74.74
Fe ₂ O ₃	0.77	1.08	0.58	0.19	0.77	0.24	0.33	0.55
FeO	2.37	2.18	2.34	1.98	2.38	3.68	2.56	1.41
Al ₂ O ₃	13.82	13.7	13.72	11.95	13.6	13.01	13.42	13.35
CaO	1.02	1.7	1.16	1.66	1.25	2.25	1.33	0.73
MgO	0.33	0.77	0.3	0.31	0.2	0.64	0.26	0.41
K ₂ O	4.72	4.03	4.98	5.19	3.58	3.78	4.96	5.2
Na ₂ O	3.77	4.23	3.87	2.85	4.5	3.42	3.83	2.77
MnO	0.08	0.08	0.08	0.04	0.14	0.07	0.07	0.04
TiO ₂	0.2	0.2	0.24	0.22	0.15	0.37	0.25	0.17
P ₂ O ₅	0.05	0.04	0.06	0.05	0.02	0.12	0.06	0.19
LOI	1.19	0.77	1.1	1.43	0.67	1.71	1.27	0.62
Total	99.47	98.69	99.87	102.28	97.99	100.53	101.18	100.18
FeO ^T	3.06	3.15	2.86	2.15	3.07	3.9	2.86	1.9
Na ₂ O + K ₂ O	8.49	8.26	8.85	8.04	8.08	7.2	8.79	7.97
A/CNK	1.45	1.38	1.37	1.23	1.46	1.38	1.33	1.53
A/NK	1.63	1.66	1.55	1.49	1.68	1.81	1.53	1.68
Mg [#]	16.11	30.34	15.74	20.44	10.4	22.65	13.96	27.73
La	25.8	13.8	63.9	42.5	24.2	33	68.5	12.7
Ce	39.9	27.1	108	72.7	47.3	60.6	110.7	23.7
Pr	5.5	4.23	11.9	7.99	6.72	7.28	12.2	3.35
Nd	18.3	16.6	38.3	26.5	26.1	27	39.9	12.5
Sm	2.62	3.64	5.58	4.06	5.07	5.12	5.52	3.32
Eu	0.55	0.59	1.07	0.59	0.7	1.05	1.04	0.33
Gd	2.21	3.62	4.23	3.29	4.47	4.29	4.19	3.07
Tb	0.36	0.8	0.63	0.55	0.77	0.8	0.63	0.66
Dy	2.06	5.28	3.39	3.14	4.23	4.65	3.09	3.52
Ho	0.44	1.21	0.64	0.63	0.81	0.97	0.61	0.56
Er	1.25	3.43	1.82	2.01	2.39	2.74	2.13	1.3
Tm	0.23	0.6	0.32	0.33	0.43	0.51	0.29	0.21
Yb	1.54	3.99	2.09	2.17	3.02	3.24	1.92	1.21
Lu	0.24	0.62	0.33	0.35	0.54	0.55	0.31	0.18
Y	8.6	30.1	18	18.7	22.8	27.6	16.9	17.1
Rb	76.2	55.5	143.3	257.1	76.7	170.4	143.7	480.8
Ba	535.9	620.1	854.4	507.7	695	734.8	782.7	219.4
Th	13.4	13.8	14.5	23.1	12.9	13.9	13.5	10.3
K	37,672.4	31,884.8	36,140.6	40,590.3	28,938	27,584.9	36,537.2	40,053.4
Sr	94.63	74.27	153	123.6	59.61	233.9	140.1	52.9
P	200	200	200.6	199.2	160	419.7	208.9	788.9
Hf	3.61	6.78	8	3.4	7.14	6.3	8.4	3
Zr	243.6	254	246.8	113.5	233.8	197.5	254.8	75.8
Ti	1209	1276	1158.1	1099.5	871.8	1824.9	1162.4	622.2
Nb	10.2	17.3	10.8	8.22	12.8	11.4	9.73	20.6
Ta	0.73	1.24	0.94	0.52	1.01	1.13	0.48	1.37
Sc	0.87	2.14	3.31	2.41	2.66	4.37	3.19	2.97
Cr	16.5	14.6	8.92	5.73	19.2	10.8	10	6.83
ΣREE	101	85.5	242.2	166.81	126.75	151.8	251.03	66.61

Table 1 continued

Sample	Moyite			Monzogranite				
	TW4-1	TW4-3	TW7-1	TW8-4	TW4-5	TW7-4	TW8-2	D90
LREE	92.67	65.96	228.75	154.34	110.09	134.05	237.86	55.9
HREE	8.33	19.55	13.45	12.47	16.66	17.75	13.17	10.71
LREE/HREE	11.12	3.37	17.01	12.38	6.61	7.55	18.06	5.22
(La/Yb) _N	12.02	2.48	21.93	14.05	5.75	7.31	25.59	7.53
(Ce/Yb) _N	7.2	1.89	14.35	9.31	4.35	5.2	16.02	5.44
(Rb/Yb) _N	3.63	1.02	5.02	8.68	1.86	3.85	5.48	29.12
δEu	0.68	0.49	0.65	0.48	0.44	0.67	0.64	0.31
δCe	0.78	0.86	0.89	0.9	0.89	0.92	0.87	0.87
Yb + Ta	2.27	5.23	3.03	2.69	4.03	4.37	2.4	2.58
La/Sm	9.85	3.79	11.45	10.47	4.77	6.45	12.41	3.83
Ba/Nb	18.8	47.4	28.8	26.92	35.6	39	26.63	37.7
La/Nb	2.53	0.8	5.92	5.17	1.89	2.89	7.04	0.62
Rb/Sr	0.81	0.75	0.94	2.08	1.29	0.73	1.03	9.09
Th/La	0.52	1	0.23	0.54	0.53	0.42	0.2	0.81
Nb*	0.091	0.149	0.089	0.042	0.118	0.098	0.086	0.238

$\text{FeO}^T = \text{FeO} + \text{Fe}_2\text{O}_3 \times 0.8998$; $\text{Mg}^\# = \text{molar } 100 \times \text{Mg}/(\text{Mg} + \text{Fe})$; A/NK = Al/Na + K in atomic ratio; A/CNK = Al/Ca + Na + K in atomic ratio; Nb* = $(\text{Nb}/\text{Th})_{\text{Sample}}/(\text{Nb}/\text{Th})_{\text{PM}}$

Shao et al. 2021) and are related to most high-K granitoids of subduction-related melt sources (e.g., Elatikpo et al. 2021).

Chondrite-normalized REE patterns of the Moyite and monzogranite samples indicate similar REE contents (85.51–242.2 and 66.61–251.03 ppm, respectively, Fig. 4a). The ratio LREE/HREE of 3.37–17.01 in moyite samples was slightly lower than 10.71–17.75 in the monzogranite samples. The degree of fractionation (La/Yb)_N in moyite ranges from 2.48 to 21.93 (average 12.14), with europium anomaly (δEu) being 0.49–0.68. The (La/Yb)_N in the monzogranite counterpart is similar (5.75–25.59, average 12.04), just as the δEu (europium anomaly) is 0.31–0.67. These rocks have similar cerium anomaly (δCe) values ranging from 0.76 to 0.89. Their REE patterns are similar in many aspects, including LREE enrichment over HREE, which corroborate their fractionated pattern.

4.2 Zircon U–Pb dating

The zircons in moyite (TW 4–3) (Fig. 5a) and monzogranite (TW 8–4) (Fig. 5b) are generally pale yellow, yellowish-brown, transparent, and euhedral. They are mostly 0.14–0.06 by 0.07–0.03 mm with aspect ratios from 2:1, 3:1, 3:2, and 5:2, often containing mineral inclusions. Cathodoluminescence images of these zircons show typical magmatic oscillation zones.

Twenty spots on zircons from moyite were analyzed for the U–Pb isotopes (Table 2). Thorium contents are from 188 to 818 ppm, with U contents as 371–987 ppm. Zircon

U–Pb ages are from 216 to 230 Ma with a calculated weighted average of 223.9 ± 2.6 Ma (Fig. 6). For the monzogranite, 13 zircons were tested, and their Th and U isotopes are 282–2147 and 601–4071 ppm, respectively. The U–Pb dates are between 218 and 235 Ma, with a calculated weighted average constrained at 226.9 ± 2.9 Ma (Fig. 6). The calculated ages of ca 224 and 227 Ma for the moyite and monzogranite, respectively, correspond to the period of Triassic magmatism in the Alanansha area.

4.3 Zircon Lu–Hf isotopes

Twelve zircon grains from the moyite (TW4-3) previously dated for U–Pb age were investigated for their Lu–Hf isotopes. The analytical results are shown in Table 3 and represented in Fig. 7.

Their $^{176}\text{Yb}/^{177}\text{Hf}$ and $^{176}\text{Hf}/^{177}\text{Hf}$ ratios are 0.014550–0.055968 and 0.282445–0.28264, respectively, with calculated εHf(t) values – 2.8 to + 0.1 except for one outlier value of –7.0, corresponding to two-stage Hf model age 1249–1437 Ga.

5 Discussion

5.1 Petrogenesis of the Alananshan intrusions

Our field investigation identified the relations between the Alananshan moyite and monzogranites to co-exist. The

Table 2 Zircon U–Pb isotope compositions of moyite and monzogranite from the Alananshan, EKOB

Sample spot no	w/10 ⁻⁶		Th/U	Isotopic ratios						Age (Ma)					
	Th	U		^{207}Pb / ^{206}Pb	1σ	^{207}Pb / ^{235}U	1σ	^{206}Pb / ^{238}U	1σ	$^{207}\text{Pb}/^{206}\text{Pb}$	1σ	$^{206}\text{Pb}/^{235}\text{U}$	1σ	$^{208}\text{Pb}/^{238}\text{U}$	1σ
<i>TW4-3 moyite</i>															
3	255	510	0.5	0.0505	0.0017	0.2462	0.0086	0.0353	0.0009	217	47	224	7	224	6
4	196	460	0.43	0.0507	0.0018	0.238	0.0084	0.034	0.0009	233	81	217	7	216	6
5	260	501	0.52	0.0505	0.0017	0.2396	0.0081	0.0344	0.0009	217	47	218	7	218	6
8	188	371	0.51	0.0522	0.0033	0.2471	0.0148	0.0346	0.0009	300	144	224	12	219	6
10	298	653	0.46	0.0499	0.0017	0.2509	0.0086	0.0364	0.001	191	78	227	7	230	6
11	523	764	0.68	0.0561	0.0021	0.2744	0.0107	0.0352	0.0009	454	114	246	9	223	6
12	227	583	0.39	0.0484	0.0017	0.2387	0.0082	0.0358	0.0009	120	81	217	7	227	6
13	200	445	0.45	0.0531	0.0018	0.2626	0.0092	0.0357	0.001	345	78	237	7	226	6
14	704	872	0.81	0.0529	0.0016	0.2625	0.0086	0.0358	0.001	324	70	237	7	227	6
15	336	659	0.51	0.0509	0.0017	0.2516	0.0085	0.0357	0.0009	239	81	228	7	226	6
16	443	619	0.72	0.0548	0.0019	0.2701	0.0092	0.0357	0.001	406	76	243	7	226	6
17	491	759	0.65	0.0543	0.0017	0.271	0.0088	0.0361	0.001	383	66	244	7	229	6
18	818	987	0.83	0.0507	0.0016	0.2433	0.0078	0.0347	0.0009	228	74	221	6	220	6
19	514	834	0.62	0.0507	0.0016	0.2482	0.008	0.0354	0.0009	228	74	225	6	224	6
20	326	588	0.55	0.0507	0.0017	0.2466	0.0081	0.0352	0.0009	233	76	224	7	223	6
21	287	555	0.52	0.0501	0.0017	0.2499	0.0084	0.0362	0.001	198	78	227	7	229	6
22	329	609	0.54	0.0506	0.0017	0.2478	0.0082	0.0354	0.0009	233	76	225	7	225	6
23	570	913	0.63	0.0	0.0016	0.2436	0.0079	0.0353	0.0009	183	74	221	6	224	6
				498											
24	740	975	0.76	0.0504	0.0016	0.2457	0.008	0.0352	0.001	213	74	223	6	223	6
26	359	623	0.58	0.0487	0.0016	0.2356	0.0078	0.0349	0.0009	132	76	215	6	221	6
<i>TW8-4 monzogranite</i>															
1	1000	2140	0.47	0.0491	0.002	0.2536	0.0105	0.0371	0.0006	154	93	229	9	235	4
3	1359	2130	0.64	0.0543	0.0019	0.2672	0.0097	0.0354	0.0005	383	82	240	8	224	3
4	1262	1794	0.7	0.055	0.0022	0.2673	0.0103	0.0352	0.0005	413	89	241	8	223	3
5	2147	2820	0.76	0.0503	0.0021	0.247	0.0104	0.0353	0.0005	209	96	224	8	224	3
6	1288	2916	0.44	0.0549	0.002	0.27	0.0098	0.0355	0.0005	409	80	243	8	225	3
9	2260	3371	0.67	0.0519	0.002	0.2622	0.0102	0.0364	0.0005	280	87	236	8	230	3
12	1510	2845	0.53	0.0535	0.0022	0.2743	0.0114	0.0372	0.0005	350	94	246	9	235	3
13	933	2198	0.42	0.0523	0.0021	0.2604	0.0102	0.0362	0.0005	298	91	235	8	229	3
14	1993	4071	0.49	0.054	0.002	0.2714	0.0106	0.0363	0.0005	372	85	244	9	230	3
15	585	889	0.66	0.0532	0.0031	0.2609	0.0156	0.0357	0.0006	339	133	235	13	226	4
17	1171	2709	0.43	0.0532	0.0022	0.2634	0.011	0.0358	0.0005	339	93	237	9	227	3
18	853	1712	0.5	0.052	0.0023	0.2473	0.0107	0.0344	0.0005	283	100	224	9	218	3
19	282	601	0.47	0.0489	0.0032	0.2454	0.0166	0.0358	0.0006	143	157	223	14	227	4

moyite occupied the core with monzogranite as the rim of the pluton. The moyite and monzogranite are pulsating in contact with clear boundaries, and a few show transitional.

Petrogenetic characteristics of granitoids are usually linked to either I-type, S-type, M-type, or A-type affinity (Chappell 1974; Whalen 1985). The Alananshan intrusive rocks have no mafic microgranular enclaves and are depleted of elements such as Nb, Mg, and Ti, which indicates that they are not M-type granites (Whalen 1985).

Compared with I- and S-type granites, A-type granites have relatively higher Zr + Nb + Ce + Y values. In the diagrams of major and trace elements (Zr + Nb + Ce + Y) versus FeO^T/MgO and $(\text{Na}_2\text{O} + \text{K}_2\text{O})/\text{CaO}$ (Fig. 8a, b), the Alananshan intrusive rocks indicate a fractionated I-type or S-type affinity, which tend to A-type granite transition. The Alananshan intrusive rocks are chemically silicic granites ($\text{SiO}_2 > 69\%$), mildly peraluminous to metaluminous, calc-alkalic to alkali-calcic. They have a

Table 3 Zircon Lu–Hf isotopes compositions of moyite from Alananshan, EKOB

Spot	$^{176}\text{Yb}/^{177}\text{Hf}$	2σ	$^{176}\text{Lu}/^{177}\text{Hf}$	2σ	$^{176}\text{Hf}/^{177}\text{Hf}$	2σ	Age(Ma)	$\varepsilon_{\text{Hf}}(0)$	$\varepsilon_{\text{Hf}}(t)$	T_{DM}
3	0.028123	0.000617	0.001656	0.000048	0.282575	0.000014	223.9	-7.0	-2.3	1403
4	0.027945	0.000398	0.001853	0.000096	0.282589	0.000016	223.9	-6.5	-1.8	1374
5	0.048261	0.000391	0.000872	0.000056	0.282561	0.000015	223.9	-7.5	-2.7	1428
11	0.024131	0.000386	0.001407	0.000007	0.28262	0.00002	223.9	-5.4	-0.7	1300
13	0.03044	0.000969	0.001249	0.000005	0.282582	0.000017	223.9	-6.7	-2.0	1384
16	0.055968	0.002763	0.002314	0.000024	0.282445	0.000018	223.9	-11.6	-7.0	1701
19	0.052921	0.001797	0.000731	0.000005	0.28264	0.000022	223.9	-4.7	0.1	1249
20	0.01455	0.000564	0.000985	0.000012	0.282566	0.000016	223.9	-7.3	-2.5	1417
22	0.023781	0.000617	0.00087	0.000011	0.282557	0.000012	223.9	-7.6	-2.8	1437
23	0.02238	0.000936	0.001324	0.000015	0.282583	0.000014	223.9	-6.7	-2.0	1382
24	0.03821	0.000278	0.00094	0.000014	0.282592	0.000013	223.9	-6.4	-1.6	1359
26	0.029924	0.002061	0.001196	0.000008	0.282576	0.000012	223.9	-6.9	-2.2	1397

where $\lambda = 1.867 \times 10^{-11} \text{ year}^{-1}$ (Söderlund et al. 2004); ($^{176}\text{Lu}/^{177}\text{Hf}$)_S and ($^{176}\text{Hf}/^{177}\text{Hf}$)_S are the measured values of the samples; ($^{176}\text{Lu}/^{177}\text{Hf}$)_{CHUR} = 0.0332 and ($^{176}\text{Hf}/^{177}\text{Hf}$)_{CHUR,0} = 0.282772 (BlichertToft et al. 1997); ($^{176}\text{Lu}/^{177}\text{Hf}$)_{DM} = 0.0384 and ($^{176}\text{Hf}/^{177}\text{Hf}$)_{DM} = 0.28325 (Nowell et al. 1998; Griffin et al. 2000); ($^{176}\text{Lu}/^{177}\text{Hf}$)_{mean crust} = 0.015, fcc = -0.548, f_{DM} = 0.16 (GERM 2001)

high-K composition (Fig. 3), often divided into S-type and I-type (Whalen et al. 1987).

Experimental studies revealed that, in metaluminous-peraluminous magma, increasing SiO₂ as the melt keeps evolving will reduce the solubility of apatite, P₂O₅, Th and Ta (Chappell 1974). This evolutionary trend is seen in the study granites from the Alananshan, where the moyite and monzogranite samples depict a geochemical trend consistent with I-type granites in the SiO₂ vs. P₂O₅ and Rb vs. Th binary diagrams (Fig. 8c, d). A mineral inventory of the rocks of Alananshan reveals the presence of phases like amphibole and biotite that usually index the I-type granitoids (Fig. 2c, e). This varies with the S-type granite characterized by aluminum-rich minerals such as muscovite and cordierite. Works of Eby (1992) and Gao et al. (2016a) have shown that when K₂O content in the rock is nearly 5 and 3.2 wt.%, the corresponding Na₂O content will be less than 3.2 and 2.2 wt.%, respectively. The A/CNK values of the moyite and monzogranite are low (< 1.16), exonerating the likely S-type granite affinity. Thus, the geochemical composition of these rocks implicates an I-type granite.

The formation of I-type granites usually has three mechanisms: (1) the mixing of mantle-derived melts and crust-derived felsic melts (Wu et al. 2007; Gray and Kemp 2009; Han et al. 2021); (2) the partial melting of lower crust metagneous rocks (Chappell and White 1992; Altherr et al. 2000; Zhou et al. 2020); (3) crystallization differentiation of mantle-derived mafic magma (Sisson et al. 2005; Nandedkar and Ulmer 2014; Zhang et al. 2015). Note that mixing of two geochemically contrasting end melts would result in obvious geochemical variation in

the resultant melt. The relatively consistent whole-rock geochemical composition of the Alananshan moyite and monzogranite contradict this mixing mechanism. Nevertheless, the consistent homogeneous whole-rock major and trace compositions could probably result from absolute mixing via magma convection caused by the long evolution time in the magma chamber. If this happens, $\varepsilon_{\text{Hf}}(t)$ values of zircon grains crystallizing from mixed melts generally show a relatively wide range of variation (up to 10 U; Davidson et al. 2007; Sun et al. 2010; Zhou et al. 2020). However, except for one outlier with an $\varepsilon_{\text{Hf}}(t)$ value of -7, the zircon Lu–Hf isotopic composition of the Alananshan moyite is relatively uniform and mostly between -2.8 and +0.2. The mixed evolution mechanism of mantle-derived and crust-derived melts cannot explain the formation of the Alananshan pluton either.

Due to the incompatibility of trace elements such as Nb, Th, Ta, and U, their distribution coefficients are close (Niu and O'Hara 2009). The Nb/Th and Ta/U ratios in mantle-derived mafic magmas are usually inherited from the source region and remain unchanged during melt evolution (Huang et al. 2014; Zhao et al. 2020). The Nb*[Nb/Th]_{Sample}/(Nb/Th)_{PM} values of 0.04 to 0.24 for the Alananshan intrusion are significantly lower than the primitive mantle. Although an enriched mantle magma mixed with crustal material was reported for the melt that crystallized into intrusion in some mining areas in EKOB (Li et al. 2018a, b), our Hf isotopes did not support the mantle source for the Alananshan granites (except for one outlier with an $\varepsilon_{\text{Hf}}(t)$ value of -7, our zircon Hf isotopes are $\varepsilon_{\text{Hf}}(t) = -2.8 \pm 0.2$). Moreover, crustal-contaminated melt does have a remnant of unassimilated xenoliths due to

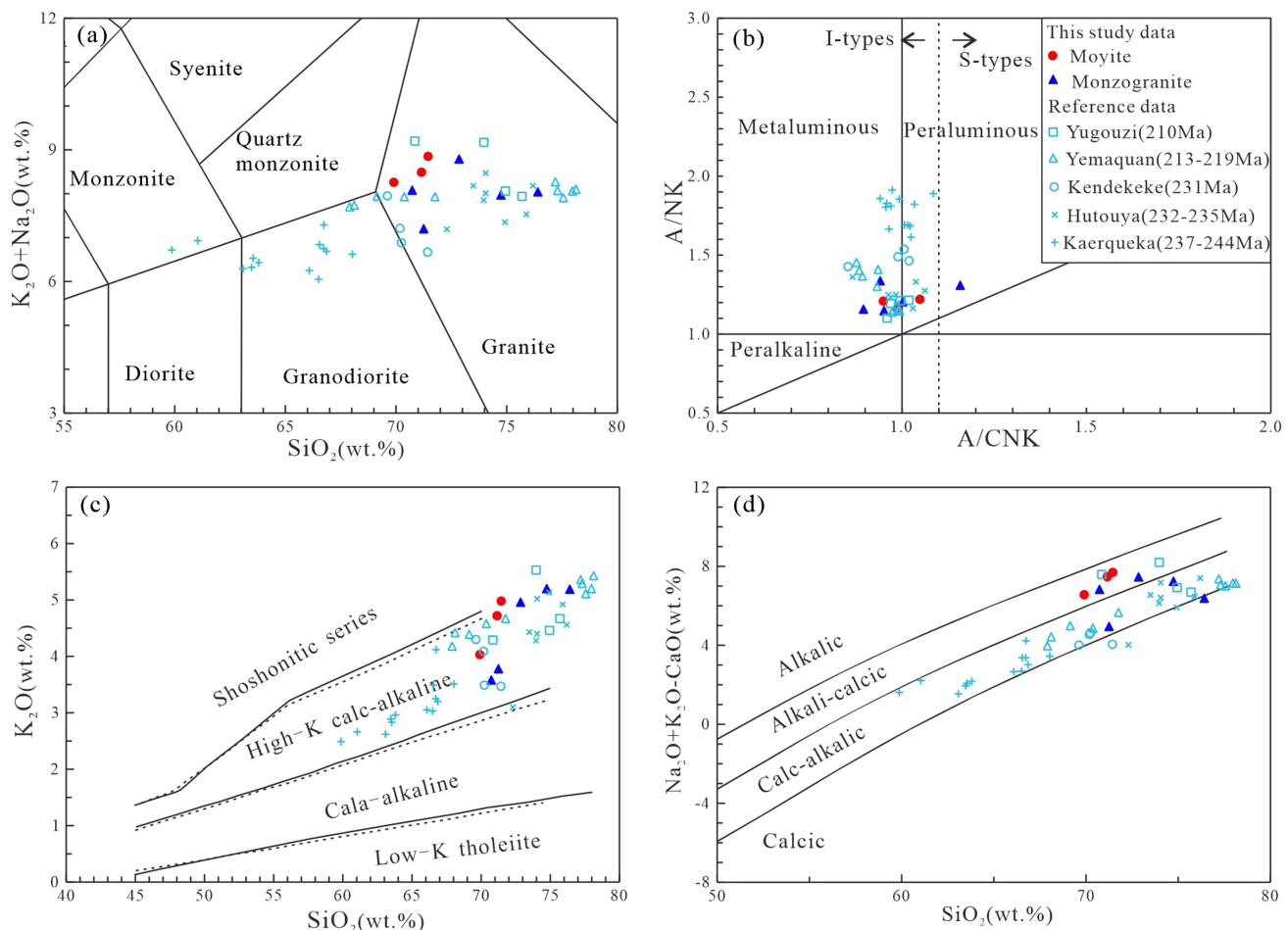


Fig. 3 Binary diagrams showing the nature of the melt that crystallized into the Alanashan intrusive rocks **a** SiO_2 vs. $\text{K}_2\text{O} + \text{Na}_2\text{O}$ (after Middlemost 1994); **b** A/NK [$\text{Al}_2\text{O}_3/(\text{Na}_2\text{O} + \text{K}_2\text{O})$] vs. A/CNK [$\text{Al}_2\text{O}_3/(\text{CaO} + \text{Na}_2\text{O} + \text{K}_2\text{O})$] (after Rickwood 1989) **c** SiO_2 vs. K_2O (after Peccerillo and Taylor 1976); and **d** SiO_2 vs. $\text{Na}_2\text{O} + \text{K}_2\text{O} - \text{CaO}$ (after Frost et al. 2001); Reference data: Yugouzi after Qian et al. 2015; Yemaquan after Gao et al. 2014; Kendekeke after Xi et al. 2010; Hutouya after Yao 2015; Kaerqueka after Wang 2009b, Yao et al. 2018; The legend is the same as the figures below

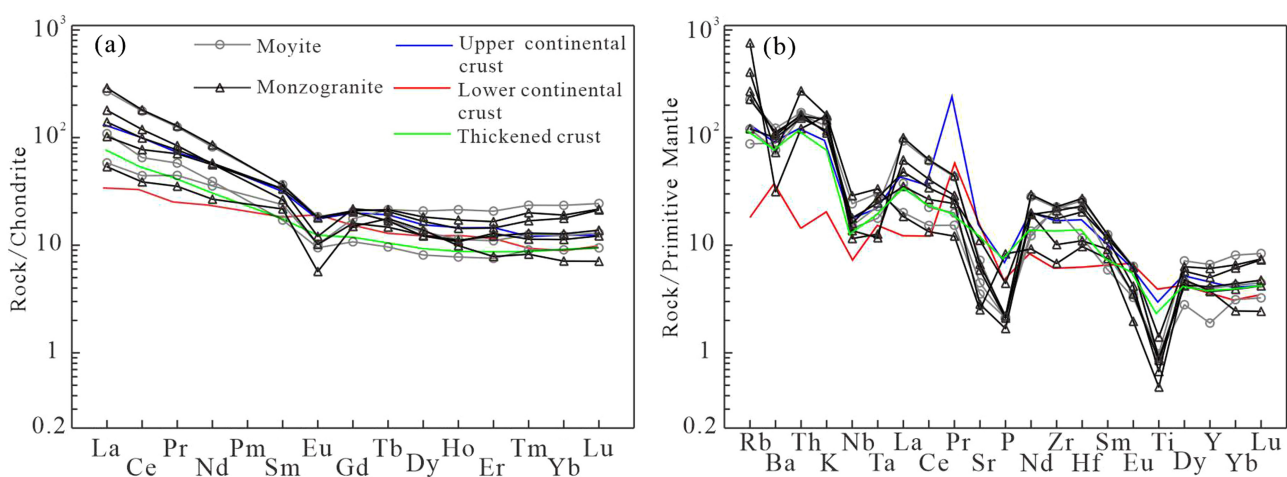


Fig. 4 Trace and REE distribution patterns in the moyite and monzogranite of the Alanashan **a** Rare earth elements and **b** Trace element (Normalization values after Sun and McDonough 1989; Crust values after Rudnick and Gao 2014; Thickened values after Zhou et al. 2020)

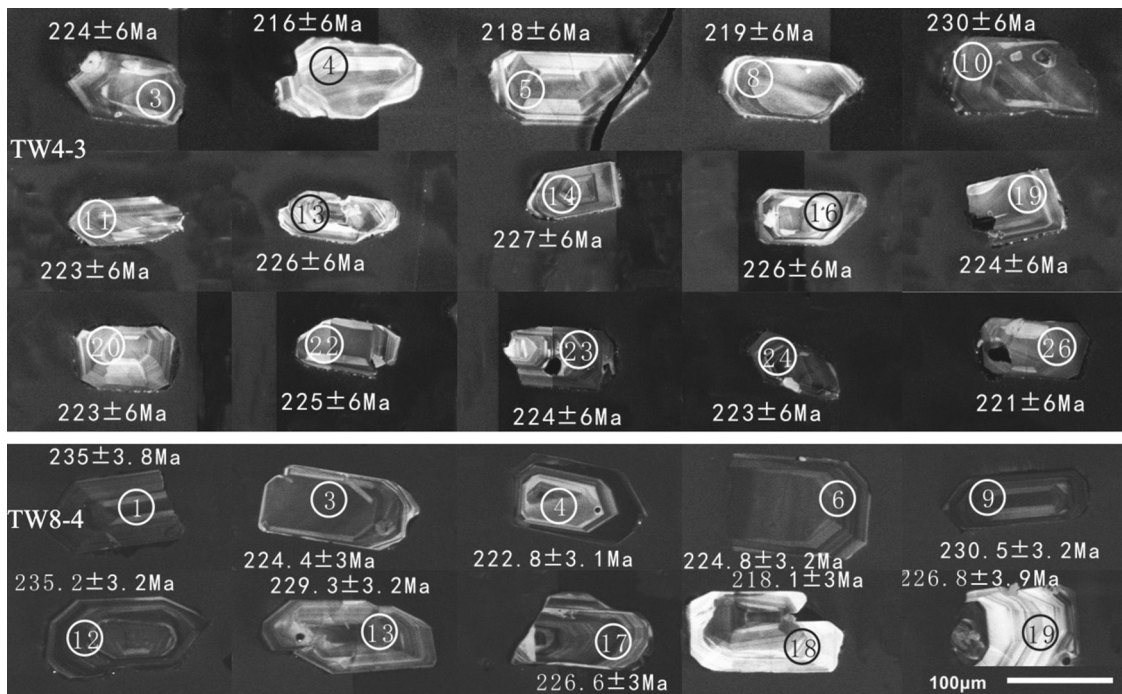


Fig. 5 Representative zircons from the moyite and monzogranite samples showing textures and laser spots

the dynamics of magma ascent, a feature not seen in the Alananshan rocks. In the $\text{SiO}_2\text{-Mg}^{\#}$ diagram (Fig. 9a), as SiO_2 increases, $\text{Mg}^{\#}$ tends to decrease, while the $\text{Mg}^{\#}$ of the melt formed by partial melting of lower crustal material is less than 45 (Guo et al. 2018). The calculated $\text{Mg}^{\#}$ values for the Alananshan intrusive rocks ranged from 10.4 to 30.34, indicating no significant interaction with mantle components. Moreover, after the differentiation of mafic magma, the volume of felsic magma is generally less than 25 %, which is inconsistent with the large volume of the Triassic felsic rocks in the EKOB. A few basic rocks of the Triassic age in the Alananshan area exist in the form of dikes and small plutons (Chen et al. 2018, 2019). Therefore, the mantle-derived magma mixed with crustal materials is not the likely melt source for the Alananshan granitoids.

The third option—partial melting of the lower crust, seems plausible for Alananshan granitoid's melt, similar to most other contemporaneous I-type granitoids in EKOB. In Fig. 9d, La positively correlated with La/Sm , indicating partial melting as the main mechanism responsible for the Alananshan granite's melt. The chondrite-normalized pattern of the Alananshan granitoids in Fig. 4a resembles those of the EKOB thickened crust and the upper crust. Similarly, the trace element normalized pattern for the Alananshan rocks overlapped those of the upper and lower crusts (Fig. 4b). The exception is the contents of Rb, Th, and Pr. Amphibole fractionation during melt evolution of the Alananshan granitoids may account for this.

The transition from middle-K calc-alkaline magma to high-K calc-alkaline magma in the Middle Triassic of Qimantag indicates that its crust thickened during the Middle Triassic (Deng et al. 2015). This, therefore, indicated the presence of an ancient basement and thickened crust in the lower crust of EKOB during the Late Triassic, which can be a potential materials source for Alananshan intrusion. However, in the $(\text{Na}_2\text{O} + \text{K}_2\text{O} + \text{FeO}^{\text{T}} + \text{MgO} + \text{TiO}_2)$ versus $(\text{Na}_2\text{O} + \text{K}_2\text{O})/(\text{FeO}^{\text{T}} + \text{MgO} + \text{TiO}_2)$ and $(\text{Al}_2\text{O}_3 + \text{MgO} + \text{FeO}^{\text{T}} + \text{TiO}_2)$ versus $\text{Al}_2\text{O}_3/(\text{MgO} + \text{FeO}^{\text{T}} + \text{TiO}_2)$ diagrams, the Alananshan samples plotted in the field defined for partial melting of amphibolite to metagreywackes (Fig. 9b, c). Research work (e.g., Huang et al. 2014; Zhou et al. 2020) has shown that, during crustal thickening, meta-igneous and sedimentary rocks in the upper crust, such as the meta-metagreywackes and amphibolites, are consumed, which may be the source of meta-aluminous I-type granite magma. The thickened lower crust was formed by partial melting of subducted Paleo-Tethys lithosphere and terrigenous sediments (Huang et al. 2014). The two-stage Hf model age of 1244–1695 Ga for the Alananshan pluton corresponds to the basement of the Mesoproterozoic Baishahe Formation, indicating derivation from a Meso-proterozoic crustal component. Therefore, we conclude that the magma source of the Alananshan granitoids is the thickened juvenile crustal material.

The Alananshan magma evolution involves the fractionation of plagioclase or other minerals. Figure 9e–f

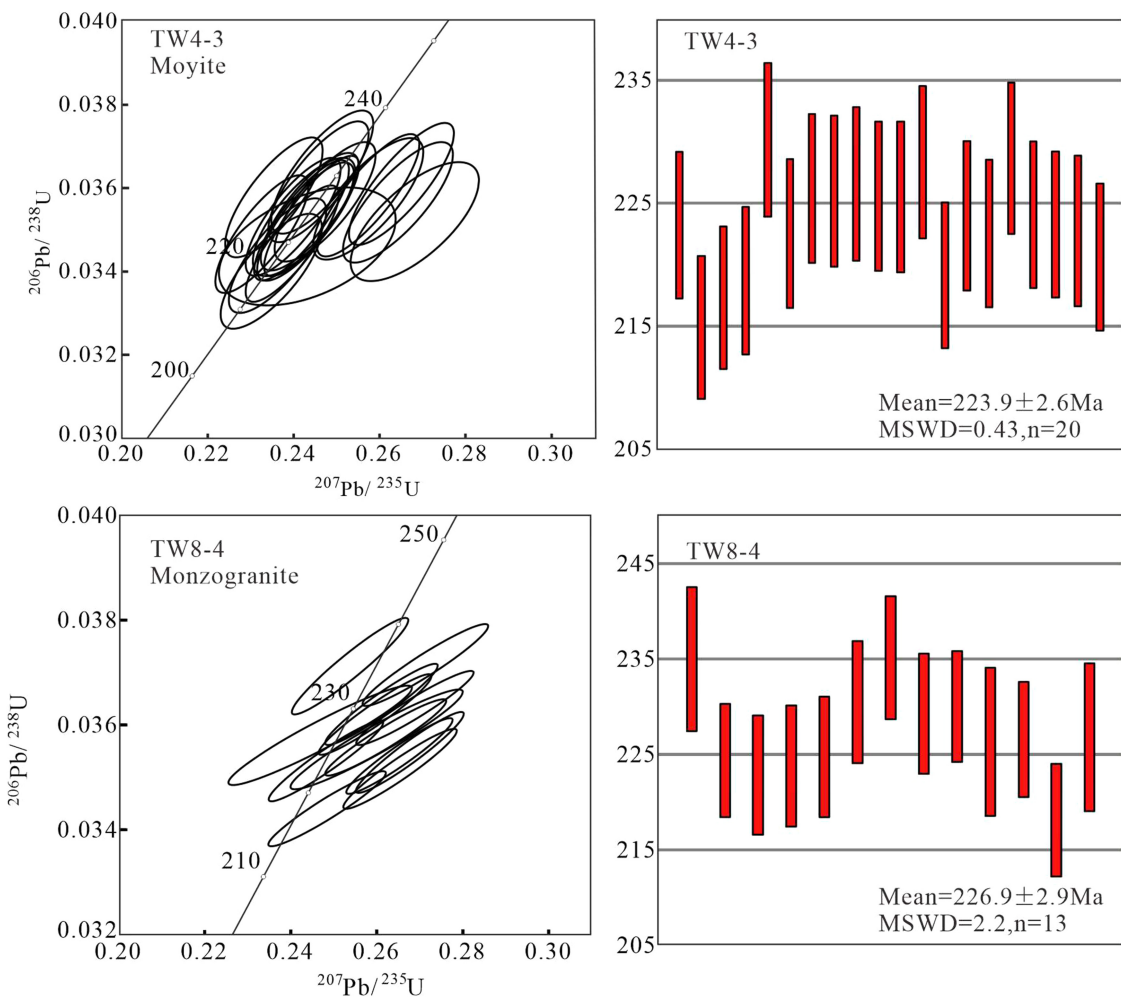


Fig. 6 Age diagrams of the moyite and monzogranite samples of the Alananshan

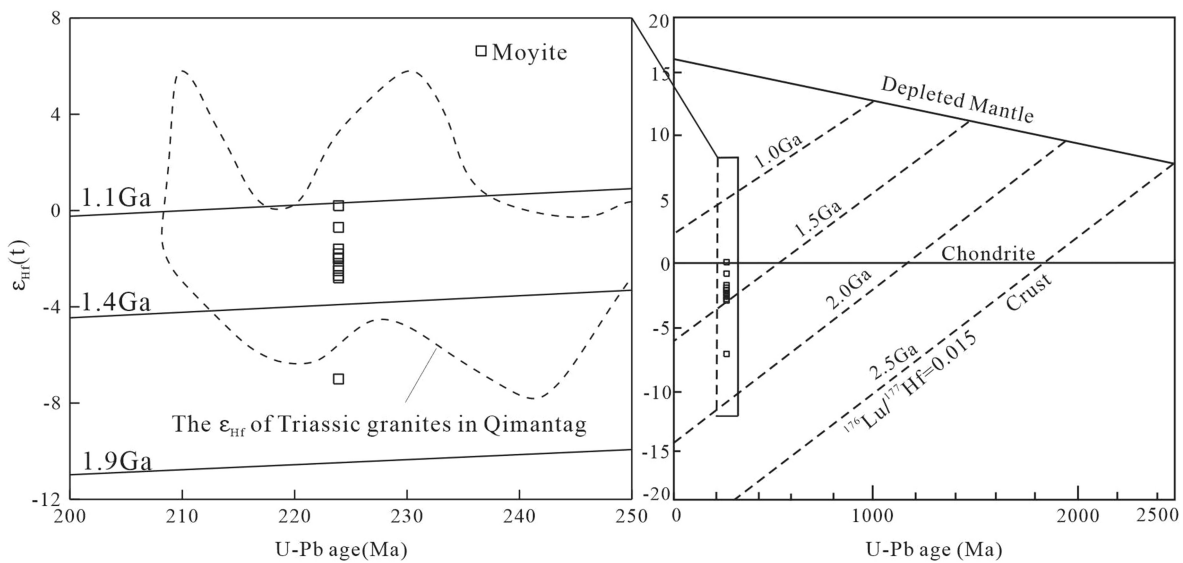


Fig. 7 U–Pb–Hf diagrams indicating the crustal isotopic signature of the Alananshan intrusive rocks (after Yang et al. 2006; Yao et al. 2017)

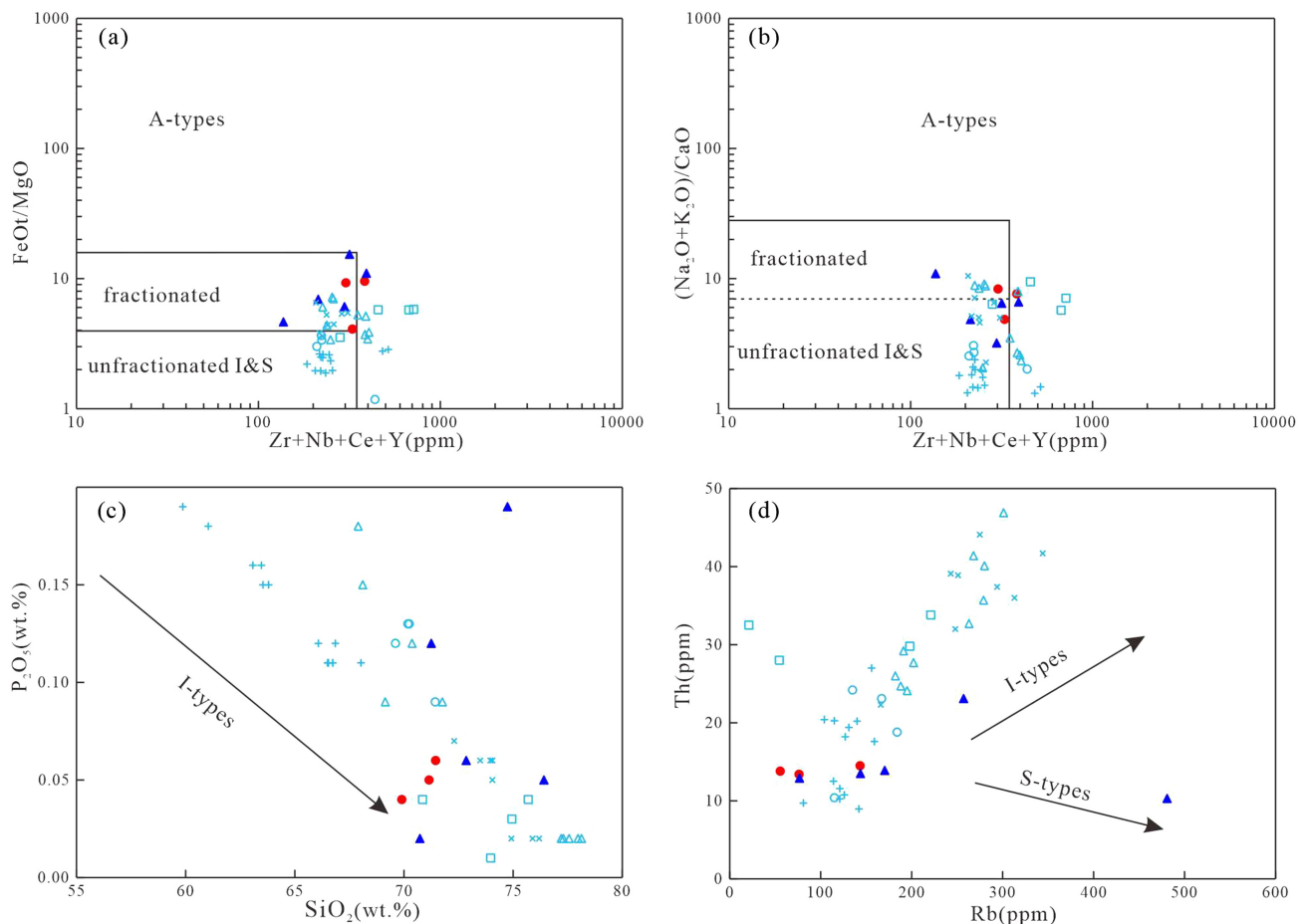


Fig. 8 Rock classification diagrams for the moyite and monzogranite of Alananshan **a** $Zr + Nb + Ce + Y$ vs. $FeOT/MgO$; **b** $Zr + Nb + Ce + Y$ vs. $K_2O + Na_2O/CaO$; **c** SiO_2 vs. P_2O_5 ; and **d** Rb vs. Th (**a**, **b** after Whalen et al. 1987)

corroborates the fractionation of plagioclase and K-feldspar as displayed in Sr vs. Rb and La/Nb vs. Ba/Nb diagrams. Strontium often replaces Ca in plagioclase and is enriched in phases like apatite and plagioclase (Guo et al. 2018). The pluton in the study area is poor in Sr, indicating fractionation of calcium-rich plagioclase, apatite and other Sr-enriched phases (Gao et al. 2016b). The SiO_2 contents in Alananshan granitoids correlate negatively with MgO , Fe_2O_3 and TiO_2 , indicating fractionation of iron-magnesium and iron-titanium oxides during the magma evolution.

Crustal thickening caused by plate subduction and thermal energy resulting from asthenospheric upwelling or mantle convection induces partial melting of the lower crust, which is critical for forming I-type granite (Barbarin 1999; Zhao et al. 2020). The calc-alkaline granite formed by the partial melting of the thickened juvenile crust and the adakite linked to the melting of the breakoff slab in EKOB in the Triassic indicates the activity of asthenospheric upwelling (Liu et al. 2017a, b; Chen et al. 2019). Therefore, we consider partial melting of the lower crust,

especially the thickened juvenile crust, by the asthenosphere upwelling as the melt source of the Alananshan pluton. It experienced the fractionation of feldspar and other minerals during its magma evolution.

5.2 Tectonic setting

Trace elements such as the Y, Yb, Ta and Rb have been used in deciphering the geotectonic setting of many igneous rocks (e.g., Pearce et al. 1984). In the Y-Nb and Yb + Ta versus Rb diagrams (Fig. 10), the Alananshan samples were plotted in the syn-collisional and volcanic arc granite regions. Compared to granite formed under compression tectonics, the REE patterns of granites formed under an extensional regime usually have a uniform downward trend, with insignificant variation in the slope of LREE and HREE, with positive or weak Eu anomaly (Wu 1995). Granite formed in an extensional setting has an inflection point at Gd, negative Eu anomaly, and relatively flat REE patterns, with a Gd/Lu ratio of 8–12, lesser than that of their equivalent collisional setting (Gd/Lu 15) (Wu

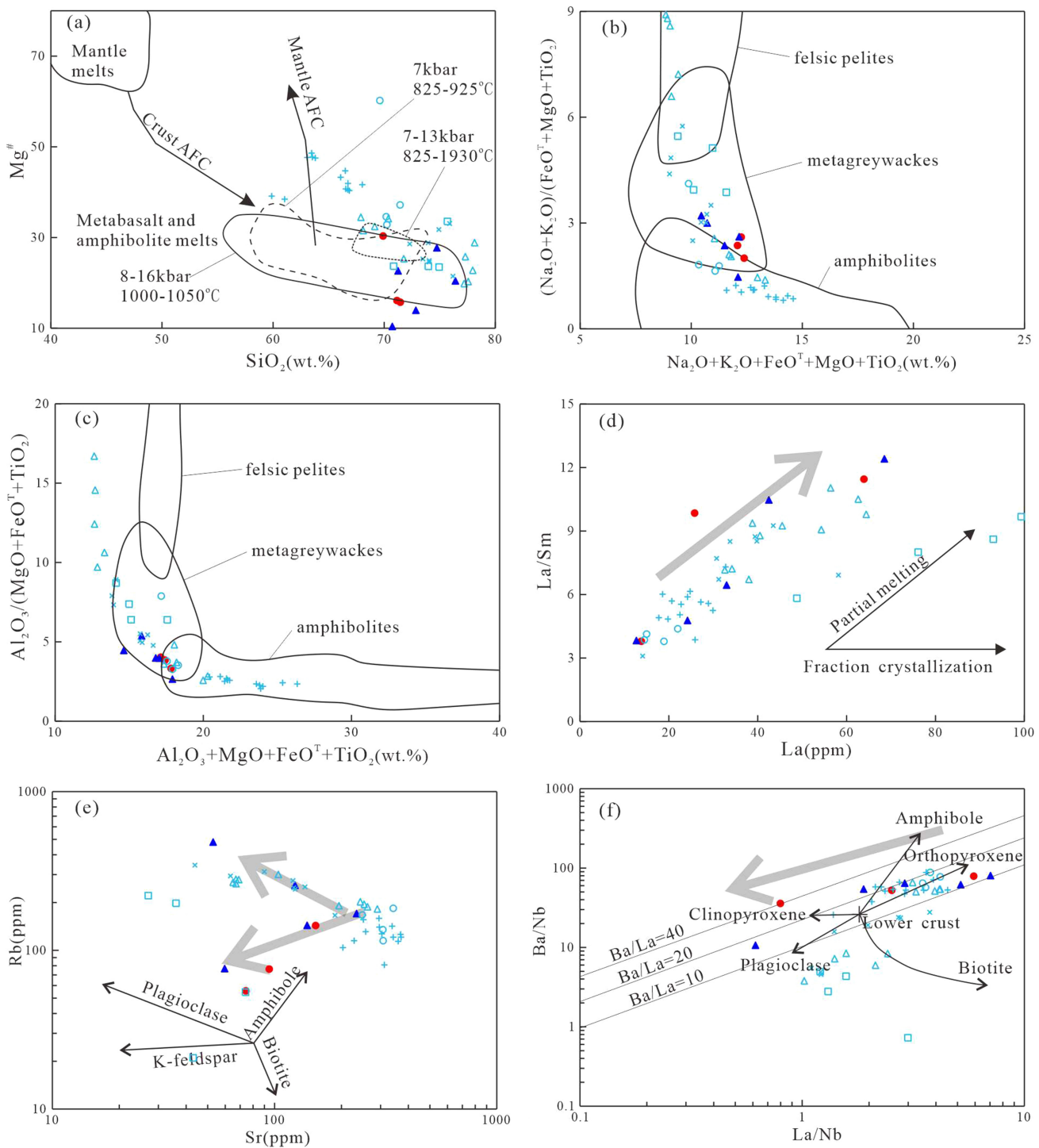


Fig. 9 Binary diagrams showing melt source and fractionating phases in the moyite and monzogranite from the Alananshan **a** SiO_2 vs. $\text{Mg}^{\#}$ (after Altherr and Siebel 2002); **b** $\text{K}_2\text{O} + \text{Na}_2\text{O} + \text{FeO}^{\text{T}} + \text{MgO} + \text{TiO}_2$ vs. $(\text{Na}_2\text{O} + \text{K}_2\text{O})/(\text{FeO}^{\text{T}} + \text{MgO} + \text{TiO}_2)$; **c** $\text{Al}_2\text{O}_3 + \text{MgO} + \text{FeO}^{\text{T}} + \text{TiO}_2$ (wt.%) vs. $\text{Al}_2\text{O}_3 / (\text{MgO} + \text{FeO}^{\text{T}} + \text{TiO}_2)$ (**b**, **c** after Patino 1999); **d** La vs. La/Sm; **e** Sr vs. Rb; and **f** La/Nb vs. Ba/Nb

1995; Xiong et al. 2014a). The Alananshan granitoids present a negative Eu anomaly, with a relatively flat HREE pattern (Gd/Lu 5.84–17.06), indicating a transitional setting between compression and extension. The samples have a high $\text{Zr} + \text{Nb} + \text{Ce} + \text{Y}$ content (Fig. 8a, b), which is a

characteristic of granitoid formed in the transitional regime (Zhou et al. 2020).

The EKOB records tectono-thermal activities that date back to the Early Paleozoic to Mesozoic (Yu et al. 2017). The tectono-magmatic events associated with the Paleo-

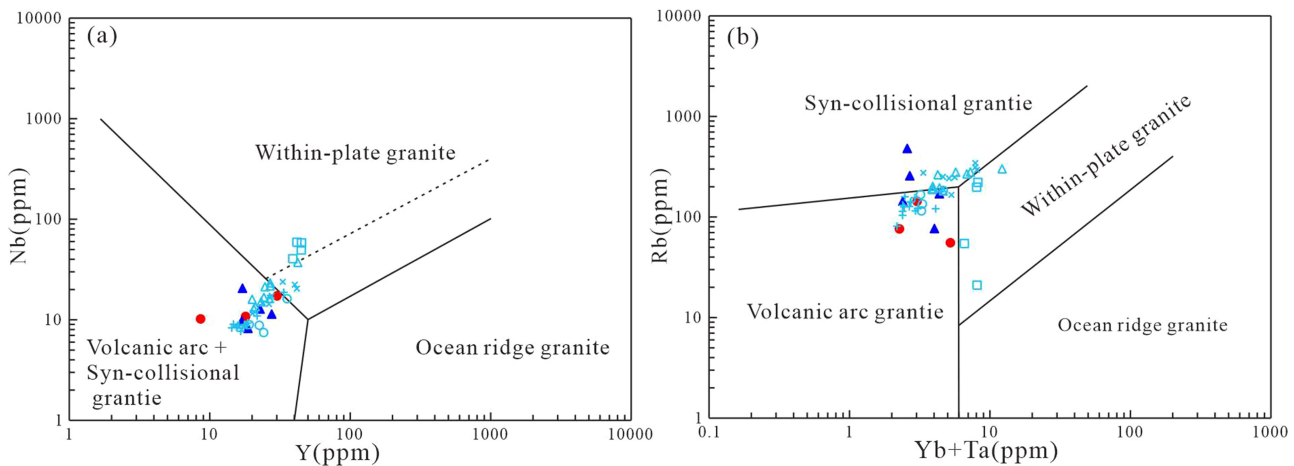


Fig. 10 Binary diagram showing the likely tectonic settings of the moyite and monzogranite from the Alananshan **a** Y vs. Nb and **b** Yb + Ta vs. Rb (after Pearce et al. 1984; Batchelor and Bowden 1985)

Tethys oceanic crust subduction and subsequent continental collision produced many late Permian to Triassic granitic magmatic rocks. The EKOB area experienced oceanic subduction, collision, and post-collision extension tectonics during this period. Although the precise timing of each event is not well constrained (Table 4), it is believed that the subduction of the Anemaqen oceanic crust started around the Middle Carboniferous, with slab exhumation at Early-Middle Triassic after subduction. The granites formed during this period are voluminous and constitute the largest intrusion in the EKOB. The post-collision event is pine to Late-Triassic to Early-Jurassic (213–204 Ma) (Table 4; Xiong et al. 2014b, 2016; Chen et al. 2015; Qian et al. 2015; Dong et al. 2018, 2020; Zhou et al. 2020). Most of the Triassic magmatic bodies in the Qimantag area are related to the large porphyry and skarn deposits, including the Yugouzi iron-rare polymetallic deposit, Yazigou polymetallic deposit, Kaerqueka copper polymetallic deposit (Fig. 1a).

Previous researches in the EKOB have linked some of the plutons to specific geodynamic settings based on their geochemistry (Table 4): (1) partial melting of an enriched mantle wedges during the Paleo-Tethys subduction to form mafic dikes, and the melting of subducting slabs mixed with lithospheric mantle-derived magma to form calc-alkaline granites (Xiong et al. 2011, 2014a; Xia et al. 2017; Chen et al. 2018; Li et al. 2020), (2) crystallization of high-K I-type granites from melt derived through melting of the ocean slab or lower crust during collision tectonics (Wu et al. 2009; Yu et al. 2015; Zhao et al. 2020; Zhou et al. 2020), and (3) crystallization of the basic dikes from upwelling asthenospheric mantle in post-collision extension setting, decompression melting of the lithospheric mantle to form some of the basic rocks, partial melting of the thickened lower crust to form the A-type granitoid, and

the adakites formed from a mixed melt from basic and crust-derived melt through underplating (Yu et al. 2015; Liu et al. 2017a, b; Chen et al. 2019).

In the Y-Nb and (Yb + Ta)-Rb tectonic discrimination diagrams (Fig. 10), the intrusive rocks in Hutouya (217.5–239.7 Ma), Yemaquan (213–229.5 Ma), and Yugouzi (210 Ma) mines mainly falls in volcanic arc and syn-collision fields which are typical of post-collision granite. Available age data (Table 4) put the period of Paleo-Tethys oceanic subduction to 240–223 Ma. The syn-to post-collisional regimes are presumed to occur during 237–204 Ma magmatism. The change from Early Triassic medium-K calc-alkaline to Middle and Late Triassic high-K calc-alkaline magmatism indicates crustal maturity variety during the transition from subduction to continental collision in Middle Triassic (Zhao et al. 2020). The folds (open to tight) and unconformable contact between Middle Triassic marine Xilikete Formation (west of the Alananshan) and Late Triassic Erlashan (Babaoshan or Duofutun) Formation (T3e, Fig. 1b) indicate the continental collisional tectonics in Middle Triassic (Li 2012; Chen et al. 2017; Zhao et al. 2020).

The crystallization of A-type granites around 237–204 Ma indicates the beginning of the extensional regime in the Late Triassic magmatism in EKOB (Liu et al. 2006; Wang et al. 2009a, b). The geochemical characteristics of the Alananshan granitoid are similar to the high-K I-type granite formed under the compression setting, formed through melting of the thickened lower crust under the post-collision extensional regime. As compiled in this study, the Alananshan granitoids in Qimantag formed mainly during the transitional regime between the period of a major collision and the extensional tectonics. The period around 223.9 Ma in the Qimantag area was still an active collisional setting (Wang et al. 2009a; Wu et al. 2009;

Table 4 The Triassic magmatism age list related to mineralization in western EKOB

Location	Lithology	Test method	Age (Ma)	Tectonic background	Literature
Galinge	Quartz monzodiorite	Zircon U–Pb LA-ICP-MS	228.3 ± 0.5	Subduction-collision transition	Gao et al. (2012)
Galinge	Quartz monzonite	Zircon U–Pb LA-ICP-MS	234.4 ± 0.6	Subduction-collision transition	Gao et al. (2012)
Galinge	Granodiorite	Zircon U–Pb LA-ICP-MS	229.4 ± 0.8	Collision	Yu (2013)
Galinge	Granite	Zircon U–Pb TIMS	227.8 ± 1.7	Post-collision	Feng et al. (2012)
Galinge	Diorite	Zircon U–Pb LA-ICP-MS	228 ± 2	Subduction-collision transition	Bai et al. (2016)
Hutouya	Granodiorite	Zircon U–Pb LA-ICP-MS	235.4 ± 1.8	Post-collision	Feng et al. (2011)
Hutouya	Monzogranite	Zircon U–Pb SHRIMP	219.2 ± 1.4	Post-collision	Feng et al. (2011)
Hutouya	Monzogranite	Zircon U–Pb LA-ICP-MS	217.5 ± 1.1	Post-collision	Zhang et al. (2013)
Hutouya	Monzogranite	Zircon U–Pb LA-ICP-MS	222.8 ± 1	Post-collision	Yao (2015)
Hutouya	Granite	Zircon U–Pb LA-ICP-MS	233.6 ± 1.8	Post-collision	Yao (2015)
Hutouya	Granite	Zircon U–Pb LA-ICP-MS	231.7 ± 2.7	Post-collision	Yao (2015)
Hutouya	Monzogranite	Zircon U–Pb LA-ICP-MS	235 ± 1.5	Post-collision	Yao (2015)
Hutouya	Granite porphyry	Zircon U–Pb LA-ICP-MS	232.7 ± 1.8	Post-collision	Zhang et al. (2016)
Hutouya	Syenite granite	Zircon U–Pb LA-ICP-MS	239.7 ± 0.8	Post-collision	Li et al. (2015)
Hutouya	Granodiorite	Zircon U–Pb LA-ICP-MS	224.3 ± 0.6	Post-collision	Li et al. (2015)
Hutouya	Monzonite	Zircon U–Pb LA-ICP-MS	234.2 ± 1.5	Subduction-collision transition	Shi et al. (2017)
Hutouya	Monzogranite	Zircon U–Pb LA-ICP-MS	230.3 ± 3.7	Post-collision	Qu et al. (2019)
Hutouya	Monzogranite	Zircon U–Pb LA-ICP-MS	221.6 ± 1.3	Post-collision	Qu et al. (2019)
Hutouya	Monzogranite	Biotite $^{40}\text{Ar}/^{39}\text{Ar}$	229.6 ± 2.3	Post-collision	Qu et al. (2019)
Hutouya	Monzogranite	Biotite $^{40}\text{Ar}/^{39}\text{Ar}$	224.7 ± 2.6	Post-collision	Qu et al. (2019)
Hutouya	Granite	Zircon U–Pb LA-ICP-MS	231.7 ± 2.1	Post-collision	Yao (2015)
Kendekeke	Monzogranite	Zircon U–Pb LA-ICP-MS	230.5 ± 4.2	Post-collision	Xi et al. (2010)
Kendekeke	Monzogranite	Zircon U–Pb LA-ICP-MS	229.5 ± 0.5	Post-collision	Xiao et al. (2013)
Kendekeke	Syenite granite	Zircon U–Pb LA-ICP-MS	217.9 ± 1.7	Post-collision	Zhang et al. (2018)
Kendekeke	Granodiorite	Zircon U–Pb LA-ICP-MS	245.1 ± 1.5	Subduction	Yao (2015)
Yemaquan	Syenite granite	Zircon U–Pb LA-ICP-MS	213 ± 1	Collision-post-collision transition	Gao et al. (2014)
Yemaquan	Quartz monzodiorite	Zircon U–Pb LA-ICP-MS	219 ± 1	Collision-post-collision transition	Gao et al. (2014)
Yemaquan	Monzonite	Zircon U–Pb LA-ICP-MS	223.5 ± 1.7	Post-collision	Yao (2015)
Yemaquan	Granodiorite	Zircon U–Pb LA-ICP-MS	220.53 ± 0.69	Collision-post-collision transition	Qiao et al. (2016)
Yemaquan	Granodiorite	Zircon U–Pb LA-ICP-MS	226 ± 2	Post-collision	Song et al. (2016)
Yemaquan	Monzogranite	Zircon U–Pb LA-ICP-MS	229.5 ± 2.2	Post-collision	Liu et al. (2017a, b)
Yemaquan	Monzonite	Zircon U–Pb LA-ICP-MS	223.5 ± 1.7	Post-collision	Yao (2015)
Yazigou	Moyite porphyry	Zircon U–Pb SHRIMP	224.0 ± 1.6	Collision-post-collision transition	Li et al. (2008)
Zharimarina	Monzogranite	Zircon U–Pb LA-ICP-MS	224.4 ± 1.9	Collision	Yao (2015)
Jingren	Syenogranite	Zircon U–Pb SHRIMP	204.1 ± 2.6	Post-collision	Liu et al. (2006)
Nalingguolehe	Moyite	Zircon U–Pb LA-ICP-MS	225.2 ± 1.2	Post-collision	Chang et al. (2009)
Wulanwuzhuer	Granite porphyry	Zircon U–Pb SHRIMP	215.1 ± 4.5	—	She et al. (2007)
Changshan	Moyite	Zircon U–Pb SHRIMP	219.9 ± 1.3	Post-collision	Feng et al. (2012)
Maxingdaban	Monzogranite	Zircon U–Pb LA-ICP-MS	218 ± 2	Collision	Wu et al. (2011)
Mohexiala	Granite porphyry	Zircon U–Pb LA-ICP-MS	222 ± 1	Post-collision	Xu et al. (2014)
Xiarihamu	Quartz diorite	Zircon U–Pb LA-ICP-MS	243 ± 1	Subduction-collision transition	Wang et al. (2014)
Tawenchahan	Granite	Zircon U–Pb LA-ICP-MS	227.7 ± 0.6	Post-collision	Feng et al. (2012)
Tawenchahan	Granodiorite	Zircon U–Pb LA-ICP-MS	233.5 ± 0.9	Post-collision	Yao (2015)
Chulutaohai	Granodiorite	Zircon U–Pb TIMS	226.4 ± 1.7	Post-collision	Feng et al. (2012)
Lalingzaohuo	Granodiorite	Zircon U–Pb LA-ICP-MS	242 ± 3.4	Subduction-collision transition	Chen et al. (2013)
Lalingzaohuo	Granodiorite	Zircon U–Pb LA-ICP-MS	250.4 ± 4	Subduction-collision transition	Chen et al. (2013)
Kaerqueka	Granodiorite	Zircon U–Pb SHRIMP	237 ± 2	Post-collision	Wang et al. (2009b)
Kaerqueka	Monzogranite	Zircon U–Pb SHRIMP	227.3 ± 1.8	Post-collision	Feng et al. (2012)

Table 4 continued

Location	Lithology	Test method	Age (Ma)	Tectonic background	Literature
Kaerqueka	Monzogranite	Biotite $^{40}\text{Ar}/^{39}\text{Ar}$	254.1 ± 1.5	Subduction-collision transition	Wang et al. (2009a)
Kaerqueka	Monzogranite	Biotite $^{40}\text{Ar}/^{39}\text{Ar}$	240.6 ± 1.6	Subduction-collision transition	Wang et al. (2009a)
Kaerqueka	Monzogranite	Biotite $^{40}\text{Ar}/^{39}\text{Ar}$	247.6 ± 1.4	Subduction-collision transition	Wang et al. (2009a)
Kaerqueka	Granodiorite	Zircon U–Pb LA-ICP-MS	244 ± 1.4	Subduction	Yao et al. (2018)
Kaerqueka	Dark enclave	Zircon U–Pb LA-ICP-MS	245 ± 1.9	Subduction	Yao et al. (2018)
Kaerqueka	Monzogranite	Zircon U–Pb LA-ICP-MS	234.4 ± 0.6	Subduction-collision transition	Gao et al. (2015)
Kaerqueka	Granodiorite	Zircon U–Pb LA-ICP-MS	234.1 ± 0.6	Subduction-collision transition	Gao et al. (2015)
Kaerqueka	Dark enclave	Zircon U–Pb LA-ICP-MS	210 ± 0.6	Post-collision	Qian et al. (2015)

Chen et al. 2019). The subsequent geologic process like crustal uplift resulted in the formation of the Qaidam Basin with the conspicuous appearance of the Altun and EKOB.

6 Conclusion

The following conclusions are drawn based on integrated mineralogical, geochronological, geochemical and isotopic studies on the granitoids in Alananshan pluton from the EKOB.

1. LA-ICP-MS zircon U–Pb dating constrained the Alananshan moyite and monzogranite at 223.9 ± 2.6 Ma and 226.9 ± 2.9 Ma, respectively. The rocks are high-K calc-alkaline series with chemical compositions akin to I-type granite.
2. Moyite and monzogranite have similar trace elements and REE distribution patterns indicative of a similar source and, as inferred from the geochemical composition, were produced from the partial melting of the thickened juvenile crust of the EKOB with fractionation of feldspar and other minerals by asthenosphere upwelling heating.
3. Considering the petrogenesis of contemporaneous felsic intrusive rocks in Qimantag of EKOB, the moyite and monzogranite in Alananshan were formed during the transition from a syn-collision (compression) to a post-collision (extensional relaxation) setting that is linked to the thickened crust area indicating that collision orogeny was still active during the Late Triassic.

Supplementary Information The online version contains supplementary material available at <https://doi.org/10.1007/s11631-022-00561-y>.

Acknowledgements This study was co-financed by the “Xinjiang Uygur Autonomous Region Central Government Returns the Price of Two Rights (K15-1-LQ06)”, the National Natural Science Foundations of China (No. 42101005), and the Research Foundation of Education Department of Hunan Province for Excellent Young

Scholars (No.19B097). We thank the two anonymous reviewers for their comments and suggestions.

Declarations

Conflict of interest On behalf of all authors, the corresponding author states that there is no conflict of interest.

References

- Altherr R, Siebel W (2002) I-type plutonism in a continental back-arc setting: miocene granitoids and monzonites from the central Aegean Sea. *Greece Contrib Mineral Petrol* 143(4):397–415
- Altherr R, Holl A, Hegner E, Langer C, Kreuzer H (2000) High-potassium, calc-alkaline I-type plutonism in the European Variscides: northern Vosges (France) and northern Schwarzwald (Germany). *Lithos* 50:51–73
- Bai YN, Sun FY, Qian Y, Liu HC, Zhang DM (2016) Zircon U–Pb geochronology and geochemistry of pyroxene diorite in Galinge iron-polymetallic deposit East Kunlun. *Glob Geol* 35(1):17–27 (**in Chinese with English abstract**)
- Barbarin B (1999) A review of the relationships between granitoid types, their origins and their geodynamic environments. *Lithos* 46(3):605–626
- Batchelor RA, Bowden P (1985) Petrogenetic interpretation of granitoid rock series using multicationic parameters. *Chem Geol* 48(1–4):43–55
- BlichertToft J, Chauvel C, Albarede F (1997) Separation of Hf and Lu for high-precision isotope analysis of rock samples by magnetic sector multiple collector ICP-MS. *Contrib Miner Petrol* 127:248–260
- Chang YY, Li JF, Zhang J, Cao SX, Li PP, Chen HQ (2009) Study of environment and chronology of Late Triassic intrusive rocks in East Nalinggele River of Qinghai. *Northwest Geol* 42(1):57–65 (**in Chinese with English abstract**)
- Chappell BW (1974) Two contrasting granite type. *Pac Geol* 8:173–174
- Chappell BW, White AJR (1992) I- and S-type granites in the Lachlan Fold Belt. *Trans R Soc Edinb Earth Sci* 83:1–26
- Chen J, Xie ZY, Li B, Li SP, Tan SX, Ren H, Zhang QM (2013) Geological and geochemical characteristics of the ore-bearing intrusions from the Lalingzahuo Mo polymetallic deposit and its metallogenetic significance. *Geol Explor* 49(5):813–824 (**in Chinese with English abstract**)
- Chen J, Wang BZ, Li B, Zhang ZQ, Qiao BX, Jin TT (2015) Zircon U–Pb ages, geochemistry, and Sr-Nd-Pb isotopic compositions of Middle Triassic granodiorites from the Kaimuqi area, East

- Kunlun, Northwest China: implications for slab breakoff. *Int Geol Rev* 57(2):257–270
- Chen JJ, Wei JH, Fu LB, Li H, Zhou H, Zhao X, Zhan XF, Tan J (2017) Multiple sources of the Early Mesozoic Gouli batholith, eastern Kunlun Orogenic Belt, northern Tibetan plateau: linking continental crustal growth with oceanic subduction. *Lithos* 29(2–3):161–178
- Chen GC, Pei XZ, Li RB, Li ZC, Pei L, Liu CJ, Chen YX, Li XB (2018) Triassic magma mixing and mingling at the eastern section of Eastern Kunlun: a case study from Xiangjiananshan granitic batholith. *Acta Petrol Sin* 34(8):2441–2480 (in Chinese with English abstract)
- Chen GC, Pei XZ, Li RB, Li ZC, Pei L, Liu CJ, Chen YX, Wang M, Gao F, Li XB (2019) Lithospheric extension to the post-collision stage of the Paleo-Tethys oceanic system in the East Kunlun Orogenic Belt: insights from Late Triassic plutons. *Earth Sci Front* 26(4):191–208 (in Chinese with English abstract)
- Davidson JP, Morgan DJ, Charlier BLA, Harlou R, Hora JM (2007) Microsampling and isotopic analysis of igneous rocks: implications for the study of magmatic systems. *Annu Rev Earth Planet Sci* 35:273–311
- Deng JF, Liu C, Feng YF, Xiao QH, Di YJ, Su SG, Zhao GC, Duan PX, Dai M (2015) On the correct application in the common igneous petrological diagrams: discussion and suggestion. *Geol Rev* 61(4):717–734 (in Chinese with English abstract)
- Dong YP, He DF, Sun SS, Liu XM, Zhou XH, Zhang FF, Yang Z, Cheng B, Zhao GC, Li JH (2018) Subduction and accretionary tectonics of the East Kunlun orogeny, western segment of the Central China Orogenic System. *Earth Sci Rev* 186:231–261
- Dong JL, Song SG, Su L, Allen MB, Li YG, Wang C (2020) Early Devonian mafic igneous rocks in the East Kunlun Orogen, NW China: implications for the transition from the Proto- to Paleo-Tethys oceans. *Lithos* 376–377:1–15
- Eby NG (1992) Chemical subdivision of the A-type granitoids: petrogenetic and tectonic implications. *Geology* 20(7):641–644
- Elatikpo SM, Li H, Zheng H, Girei MB, Wu J, Amuda AK (2021) Cryogenian crustal evolution in western Nigeria shield: whole-rock geochemistry, Sr–Nd, and zircon U–Pb–Hf isotopic evidence from Bakoshi–Gadanya granites. *Int Geol Rev*. <https://doi.org/10.1080/00206814.2021.1998799>
- Feng CY, Wang XP, Shu XF, Zhang AK, Xiao Y, Liu JN, Ma SC, Li GC, Li DX (2011) Isotopic chronology of the Hutouya skarn lead-zinc polymetallic ore district in Qimantage Area of Qinghai Province and its geological significance. *J Jilin Univ (Earth Sci Edn)* 41(6):1806–1816 (in Chinese with English abstract)
- Feng CY, Wang S, Li GC, Ma SC, Li DS (2012) Middle to Late Triassic granitoids in the Qimantage area, Qinghai Province, China: chronology, geochemistry and metallogenesis significances. *Acta Petrol Sin* 28(2):665–678 (in Chinese with English abstract)
- Frost BR, Barnes CG, Collins WJ, Arculus RJ, Ellis DJ, Frost CD (2001) A geochemical classification for granitic rocks. *J Petrol* 42(11):2033–2048
- Gao YB, Li WY, Ma XG, Zhang ZW, Tang QY (2012) Genesis, geochronology and Hf isotopic compositions of the magmatic rocks in Galinge iron deposit, eastern Kunlun. *J Lanzhou Univ (nat Sci)* 48(2):36–47 (in Chinese with English abstract)
- Gao YB, Li WY, Qian B, Li K, Li DS, He SY, Zhang ZW, Zhang JW (2014) Geochronology, geochemistry and Hf isotopic compositions of the granitic rocks related with iron mineralization in Yemaquan deposit, East Kunlun, NW China. *Acta Petrol Sin* 30(6):1647–1665 (in Chinese with English abstract)
- Gao YB, Li K, Qian B, Li WY, Li DS, Su SS, Zhang CG, Zhang DM, Wang SM (2015) The genesis of granodiorites and dark enclaves from Kaerqueka deposit in east Kunlun belt: evidence from zircon U–Pb dating, geochemistry and Sr–Nd–Hf isotopic compositons. *Geol China* 42(3):646–662 (in Chinese with English abstract)
- Gao P, Zheng YF, Zhao ZF (2016a) Distinction between S-type and peraluminous I-type granites: zircon versus whole-rock geochemistry. *Lithos* 258–259:77–91
- Gao P, Zheng YF, Zhao ZF (2016b) Experimental melts from crustal rocks: a lithochemical constraint on granite petrogenesis. *Lithos* 266–267:133–157
- Gray CM, Kemp AIS (2009) The two-component model for the genesis of granitic rocks in southeastern Australia—nature of the metasedimentary-derived and basaltic end members. *Lithos* 111:113–124
- Griffin WL, Pearson NJ, Belousova EA, Jackson SE, van Achterbergh E, O'Reilly SY, Shee SR (2000) The Hf isotope composition of cratonic mantle: LAM-MC-ICPMS analysis of zircon megacrysts in kimberlites. *Geochim Cosmochim Acta* 64:133–147
- Guo XZ, Li YZ, Jia QZ, Li JC, Kong HL, Namkha N (2018) Geochronology and geochemistry of the Wulonggou orefield related granites in Late Permian-Triassic East Kunlun: implication for metallogenic tectonic. *Acta Petrol Sin* 34(8):2359–2379 (in Chinese with English abstract)
- Han ZH, San FY, Tian N, Gao HC, Li L, Zhao TF (2021) Zircon U–Pb geochronology, geochemistry and geological implications of the early paleozoic wulanwuzhuer granites in the Qimantag, East Kunlun, China. *Earth Sci* 46(1):13–30 (in Chinese with English abstract)
- Huang H, Niu YL, Nowell G, Zhao ZD, Yu XH, Zhu DC, Mo XX, Ding S (2014) Geochemical constraints on the petrogenesis of granitoids in the East Kunlun Orogenic belt, northern Tibetan Plateau: implications for continental crust growth through syn-collisional felsic magmatism. *Chem Geol* 370:1–18
- Jackson SE, Pearson NJ, Griffin WL, Belousova EA (2004) The application of laser ablation-inductively coupled plasma-mass spectrometry to in situ U–Pb zircon geochronology. *Chem Geol* 211:47–69
- Jiang CF, Yang JS, Feng BG, Zhu ZZ, Zhao M, Chai YC (1992) Opening–closing tectonic of Kunlun Mountains. Geological Publishing House, Beijing, pp 154–161
- Li SJ, Sun FY, Feng CY, Liu ZY, Zhao JW, Li YC, Wang S (2008) Geochronology study on Yazigou polymetallic deposit in Eastern Kunlun, Qinghai Province. *Acta Geol Sin* 82(7):949–955 (in Chinese with English abstract)
- Li XH, Long WG, Li QL, Liu Y, Zheng YF, Yang YH, Chamberlain KR, Wan DF, Guo CH, Wang XC, Tao H (2010) Penglai zircon megacryst: a potential new working reference for microbeam analysis of Hf–O isotopes and U–Pb age. *Geostand Geoanal Res* 34:117–134
- Li XH, Tang GQ, Gong B, Yang HY, Hou KJ, Hu ZC, Li QL, Liu Y, Li WX (2013) Qinghu zircon: a working reference for microbeam analysis of U–Pb age and Hf and O isotopes. *Chin Sci Bull* 58:1954–1961
- Li K, Gao YB, Qian B, He SY, Liu YL, Zhang ZW, Zhang JW, Wang YL (2015) Geochronology, geochemical characteristics and Hf isotopic compositions of granite in the Hutouya deposit, Qimantag, East Kunlun. *Geol China* 42(3):630–645 (in Chinese with English abstract)
- Li RB, Pei XZ, Li ZC, Pei L, Chen GC, Chen YX, Liu CJ, Wang SM (2018a) Paleo-Tethys Ocean subduction in eastern section of East Kunlun Orogen: evidence from the geochronology and geochemistry of the Wutuo pluton. *Acta Petrol Sin* 34(11):3399–3421 (in Chinese with English abstract)
- Li RB, Pei XZ, Pei L, Li ZC, Chen GC, Chen YX, Liu CJ, Wang M (2018b) The Early Triassic Andean-type Halagatu granitoids pluton in the East Kunlun orogen, northern Tibet Plateau: response to the northward subduction of the Paleo-Tethys Ocean. *Gondwana Res* 62:212–226

- Li YJ, Wei JH, Santosh M, Li H, Liu HW, Niu MW, Liu B (2020) Anisian granodiorites and mafic microgranular enclaves in the eastern Kunlun Orogen, NW China: insights into closure of the eastern Paleo-Tethys. *Geol J* 55(9):6487–6507
- Li RB (2012) Research on the late paleozoic-early mesozoic orogeny in East Kunlun Orogen. (Doctor). Chang'an University, pp 1–185 (in Chinese with English abstract)
- Liu YH, Mo XX, Yu XH, Zhang XT, Xu GW (2006) Zircon SHRIMP U-Pb dating of the Jingren granite, Yemaquan region of the Kunlun and its geological significance. *Acta Petrol Sin* 22(10):2457–2463 (in Chinese with English abstract)
- Liu B, Ma CQ, Huang J, Wang LX, Zhao SQ, Yan R, Sun Y, Xiong FH (2017a) Petrogenesis and tectonic implications of Upper Triassic appinite dykes in the East Kunlun orogenic belt, northern Tibetan Plateau. *Lithos* 284:766–778
- Liu JN, Feng CY, He SY, Pei RF, Li DX, Zhai HY, Bai SL (2017b) Zircon U-Pb and Phlogopite Ar-Ar ages of the Monzogranite from Yemaquan Iron-zinc Deposit in Qinghai Province. *Geotect Metall* 41(6):1158–1169 (in Chinese with English abstract)
- Ludwig KR (2003) User's Manual for Isoplots 3.0. A geochronological toolkit for Microsoft Excel. Kenneth R. Ludwig
- McCulloch MT, Rosman KJR, De Laeter JR (1977) The isotopic and elemental abundance of ytterbium in meteorites and terrestrial samples. *Geochim Cosmochim Acta* 41(12):1703–1707
- Meng FC, Cui MH, Wu XK, Ren YF (2013) Heishan mafic-ultramafic rocks in the Qimantag area of Eastern Kunlun, NW China: remnants of an early paleozoic incipient island arc. *Gondwana Res* 27(2):745–759
- Middlemost EAK (1994) Naming materials in the magma/igneous rock system. *Earth Sci Rev* 37(3–4):215–224
- Mo XX, Luo ZH, Deng JF, Yu XH, Liu CD, Chen HW, Yuan WM, Liu YH (2007) Granitoids and crustal growth in the East-Kunlun Orogenic Belt. *Geol J China Univ* 13(3):403–414 (in Chinese with English abstract)
- Nandedkar RH, Ulmer P (2014) Fractional crystallization of primitive, hydrous arc magmas: an experimental study at 07 GPa. *Contrib Mineral Petrol* 167:1015
- Niu YL, O'Hara MJ (2009) MORB mantle hosts the missing Eu (Sr, Nb, Ta and Ti) in the continental crust: New perspectives on crustal growth, crust-mantle differentiation and chemical structure of oceanic upper mantle. *Lithos* 112:1–17
- Nowell GM, Kempton PD, Noble SR, Fitton JG, Saunders AD, Mahoney JJ, Taylor RN (1998) High precision Hf isotope measurements of MORB and OIB by thermal ionisation mass spectrometry: insights into the depleted mantle. *Chem Geol* 149:211–233
- Patino DAE (1999) What do experiments tell us about the relative contributions of crust and mantle to the origin of granitic magmas. *Geol Soc Spec Public* 168:55–75
- Pearce J, Harris N, Tindle AG (1984) Trace element discrimination diagrams for the tectonic interpretation of granitic rocks. *J Petrol* 25(4):956–983
- Peccerillo A, Taylor SR (1976) Geochemistry of Eocene calc-alkaline volcanic rocks from the Kastamonu area, Northern Turkey. *Contrib Miner Petrol* 58:63–81
- Qian B, Gao YB, Li K, Zhang ZW, Zhou AS, Wu YS (2015) Zircon U-Pb-Hf isotopes and whole rock geochemistry constrains on the petrogenesis of iron-rare metal mineralization related alkaline granitic intrusive rock in Yugouzi area, eastern Kunlun, Xinjiang. *Acta Petrol Sin* 31(9):2508–2520 (in Chinese with English abstract)
- Qiao BX, Pan T, Chen J (2016) Geochronology, geochemical characteristics and geological significance of granodiorite in Yemaquan iron polymetallic deposit of the East Kunlun. *J Qinghai Univ (Nat Sci Edn)* 34(1):63–73 (in Chinese with English abstract)
- Qu HY, Friehauf K, Santosh M, Pei RF, Li DX, Liu JN, Zhou SM, Wang H (2019) Middle-late Triassic magmatism in the Hutouya Fe-Cu-Pb-Zn deposit, East Kunlun Orogenic Belt, NW China: implications for geodynamic setting and polymetallic mineralization. *Ore Geol Rev* 113:1–16
- Rickwood PC (1989) Boundary lines within petrologic diagrams which use oxides for major and minor elements. *Lithos* 22(4):247–263
- Rudnick RL, Gao S (2014) Composition of the continental crust. *Treat Geochem* 4:1–51
- Santosh M, Hu CN, He XF, Li SS, Tsunogae T, Shaji E, Indu G (2017) Neoproterozoic arc magmatism in the southern Madurai Block, India: subduction, relamination, continental outbuilding, and the growth of Gondwana. *Gondwana Res* 45:1–42. <https://doi.org/10.1016/j.gr.2016.12.009>
- Shao F, Niu Y, Kong J, Liu Y, Wang G, Zhang Y (2021) Petrogenesis and tectonic implications of the Triassic rhyolites in the East Kunlun Orogenic Belt, northern Tibetan Plateau. *Geosci Front* 12(6):101243. <https://doi.org/10.1016/j.gsf.2021.101243>
- She HQ, Zhang DQ, Jing XY, Guan J, Zhu HP, Feng CY, Li DX (2007) Geological characteristics and genesis of the Ulanuzhuer porphyry copper deposit in Qinghai. *Geol China* 34(2):306–314 (in Chinese with English abstract)
- Shi C, Li RS, He SP, Ji WH, Gu PY, Chen SJ, Zhang HD (2017) A study of the ore-forming age of the Hutouya deposit and its geological significance: geochemistry and U-Pb zircon ages of biotite monzonitic granite in Qimantag, East Kunlun Mountains. *Geol Bull China* 36(6):977–986 (in Chinese with English abstract)
- Sisson TW, Ratajeski K, Hankins WB, Glazner AF (2005) Voluminous granitic magmas from common basaltic sources. *Contrib Miner Petrol* 148:635–661
- Sláma J, Košler J, Condon DJ, Crowley JL, Gerdes A, Hanchar JM, Horstwood MSA, Morris GA, Nasdala L, Norberg N, Schaltegger U, Schoene B, Tubrett MN, Whitehouse MJ (2008) Plešovice zircon—a new natural reference material for U-Pb and Hf isotopic microanalysis. *Chem Geol* 249:1–35
- Söderlund U, Patchett PJ, Vervoort JD, Isachsen CE (2004) The ^{176}Lu decay constant determined by Lu-Hf and U-Pb isotope systematics of Precambrian mafic intrusions. *Earth Planet Sci Lett* 219:311–324
- Song ZB, Zhang YL, Jia QZ, Chen XY, Jiang L, He SY, Li JC, Yang T, Quan SC, Zhang XF, Li YZ, Tang Z (2016) LA-ICP-MS zircon U-Pb age of the Yemaquan granodiorite in the Qimantag area, Qinghai Province and its geological implications. *Geol Bull China* 35(12):2006–2013 (in Chinese with English abstract)
- Sun SS, McDonough WF (1989) Chemical and isotopic systematics of oceanic basalts: implications for mantle composition and processes. *Geol Soc Lond, Spec Public* 42(1):313–345
- Sun JF, Yang JH, Wu FY, Li XH, Yang YH, Xie LW, Wilde SA (2010) Magma mixing controlling the origin of the Early Cretaceous Fangshan granitic pluton, North China Craton: in situ U-Pb age and Sr-, Nd-, Hf- and O-isotope evidence. *Lithos* 120:421–438
- Wang BC, Luo ZH, Li HY, Chen HW, Hu XL (2009a) Petro-tectonic assemblages and temporal-spatial framework of the Late Paleozoic-Early Mesozoic intrusions in the Qimantage Corridor of the East Kunlun belt. *Geol China* 36(4):769–782 (in Chinese with English abstract)
- Wang S, Feng CY, Li SJ, Jiang JH, Li DS, Su SS (2009b) Zircon SHRIMP U-Pb dating of granodiorite in the Kaerqueka polymetallic ore deposit, Qimantage Mountain, Qinghai Province, and its geological implications. *Geol China* 36(1):74–84 (in Chinese with English abstract)
- Wang G, Sun FY, Li BL, Li SJ, Zhao JW, Yang QA (2014) Zircon U-Pb geochronology and geochemistry of Diorite in Xiarihamu Ore

- District from East Kunlun and Its geological significance. *J Jilin Univ (Earth Sci Edn)* 44(3):876–891 (in Chinese with English abstract)
- Whalen JB (1985) Geochemistry of an island-arc plutonic suite: the Uasila-Yau Intrusive Complex, New Britain. *PNG J Petrol* 26(3):603–632
- Whalen JB, Currie KL, Chappell BW (1987) A-type granites: geochemical characteristics, discrimination and petrogenesis. *Contrib Miner Petrol* 95(4):407–419
- Woodhead JD, Herdt JM (2005) A preliminary appraisal of seven natural zircon reference materials for in situ Hf isotope determination. *Geostand Geoanal Res* 29:183–195
- Wu TR (1995) Granites and their tectonic setting. *Acta Scientiarum Naturalium Universitatis Pekinensis* 31(3):358–365 (in Chinese with English abstract)
- Wu FY, Li XH, Yang JH, Zheng YF (2007) Discussions on the petrogenesis of granites. *Acta Petrol Sinica* 23(6):1217–1238 (in Chinese with English abstract)
- Wu YZ, Wang Z, Guo L, Xiao PX (2009) Tectonic constraint on temporal and spatial variation of granitoid rocks in the Qimantag region, Eastern Kunlun—evidence from the changes of Potassium and Sodium contents. *Acta Geol Sin* 83(7):964–981 (in Chinese with English abstract)
- Wu XK, Meng FC, Xu H, Cui MH (2011) Zircon U-Pb dating, geochemistry and Nd-Hf isotopic compositions of the Maxingdaban Late Triassic granitic pluton from Qimantag in the eastern Kunlun. *Acta Petrol Sin* 27(11):3380–3394 (in Chinese with English abstract)
- Xi RG, Xiao PX, Wu YZ, Dong ZC, Guo L, Gao XF (2010) The geological significances, composition and age of the monzonitic granite in Kendekeke iron mine. *Northwest Geol* 43(4):195–202 (in Chinese with English abstract)
- Xia MZ, Fan YZ, Xia ZD, Rui HC, Jiang CY (2017) Geochronology, geochemical and characteristics and ore-forming conditions of the Dalakuan mafic-ultramafic intrusion, East Kunlun. *Xinjiang Acta Petrologica Sinica* 34(8):2380–2392 (in Chinese with English abstract)
- Xiao Y, Feng CY, Liu JN, Yu M, Zhou JH, Li DX, Zhao YM (2013) LA-MC-ICP-MS zircon U-Pb dating and sulfur isotope characteristics of Kendekeke Fe-polymetallic deposit Qinghai Province. *Mineral Depos* 32(1):177–186 (in Chinese with English abstract)
- Xiong FH, Ma CQ, Zhang JY, Liu B (2011) LA-ICP-MS zircon U-Pb dating, elements and Sr-Nd-Hf isotope geochemistry of the Early Mesozoic mafic dyke swarms in East Kunlun orogenic belt. *Acta Petrol Sin* 27(11):3350–3364 (in Chinese with English abstract)
- Xiong FH, Ma CQ, Jiang HA, Liu B, Huang J (2014a) Geochronology and geochemistry of Middle Devonian mafic dykes in the East Kunlun orogeny belt, Northern Tibet Plateau: Implications for the transition from Prototethys to paleotethys orogeny. *Geochimistry* 74(2):225–235
- Xiong FH, Ma CQ, Zhang JY, Liu B (2014b) Reworking of old continental Lithosphere: an important crustal evolution mechanism in orogenic belts, as evidenced by Triassic I-type granitoids in the East Kunlun orogen, Northern Tibetan Plateau. *J Geol Soc* 171(6):847–863
- Xiong FH, Ma CQ, Jiang HA, Zhang H (2016) Geochronology and petrogenesis of Triassic high-K calc-alkaline granodiorites in the East Kunlun orogen, West China: Juvenile lower crustal melting during post-collisional extension. *J Earth Sci* 27(3):474–490
- Xu QL, Sun FY, Li BL, Qian Y, Li L, Yang YQ (2014) Geochronological dating, geochemical characteristics and tectonic setting of the granite-porphyry in the Mohexiala Silver polymetallic deposit, Eastern Kunlun Orogenic Belt. *Geotecton Metall* 38(2):421–433 (in Chinese with English abstract)
- Yang JH, Wu FY, Shao JA, Wilde SA, Xie LW, Liu XM (2006) Constraints on the timing of uplift of the Yanshan fold and thrust belt, North China. *Earth Planet Sci Lett* 246(3–4):336–352
- Yao L, Lu ZC, Zhao CS, Pang ZS, Yu XF, Yang T, Li YS, Liu P, Zhang MC (2017) Zircon U-Pb geochronological, trace element, and Hf isotopic constraints on the genesis of the Fe and Cu skarn deposits in the Qiman Tagh area, Qinghai Province, Eastern Kunlun Orogen, China. *Ore Geol Rev* 91:387–403
- Yao L, Dong SY, Lu ZC, Zhao CS, Pang ZS, Yu XF, Xue JL, Geng L, Zhang ZH (2018) Origin of the Late Permian gabbros and Middle Triassic granodiorites and their mafic microgranular enclaves from the Eastern Kunlun Orogen Belt: implications for the subduction of the Palaeo-Tethys Ocean and continent-continent collision. *Geol J* 55(1):147–172
- Yao L (2015) Petrogenesis of the Triassic granitoids and skarn mineralization in the Qimantag area, Qinghai Province, and their geodynamic setting. [PhD thesis]. Beijing: China University of Geosciences (Beijing), pp 10–81 (in Chinese with English abstract)
- Yin S, Ma CQ, Xu JN (2017) Geochronology, geochemical and Sr-Nd-Hf-Pb isotopic compositions of the granitoids in the Yemaquan orefield, East Kunlun orogenic belt, northern Qinghai Tibet Plateau: implications for magmatic fractional crystallization and sub-solidus hydrothermal alteration. *Lithos* 294:339–355
- Yu M, Feng CY, Zhao YM, Li DX (2015) Genesis of post-collisional calc-alkaline and alkaline granitoids in Qimantagh, East Kunlun, China. *Lithos* 239:45–59
- Yu M, Feng CY, He SY, Zhao MQ, Zhao YM, Li DX, Qu HY, Liu JN, Wang H, Zhou JH, Zhong SH (2017) The Qiman Tagh Orogen as a window to the crustal evolution of the Northern Tibetan Plateau. *Acta Geol Sin* 91(4):703–723 (in Chinese with English abstract)
- Yu M (2013) Geochemistry and Zonation of the Glinge iron deposit, Qinghai Province [Master degree thesis]. Beijing: China University of Geosciences (Beijing), pp 59–71 (in Chinese with English abstract)
- Zhang AK, Liu GL, Feng CY, Mo XX, Yang LC, Liu YL, He SY, Ma YS (2013) Geochemical characteristics and ore-controlling factors of Hutouya polymetallic deposit. *Mineral Depos* 32(1):94–108 (in Chinese with English abstract)
- Zhang DH, Wei JH, Fu LB, Chen HY (2015) Formation of the Jurassic Changboshan-Xieniqishan highly fractionated I-type granites, north-eastern China: implication for the partial melting of juvenile crust induced by as-thenospheric mantle upwelling. *Geol J* 50(2):122–138
- Zhang XF, Li ZM, Jia QZ, Song ZB, Chen XY, Zhang YL, Li DS, Shu XF (2016) Geochronology, geochemistry and geological significance of granite porphyry in Hutouya polymetallic deposit, Qimantage area Qinghai Province. *J Jilin Univ (Earth Sci Edn)* 46(3):749–765 (in Chinese with English abstract)
- Zhang MY, Feng CY, Wang H, Li DX, Qu HY, Liu JN, Zhou JH (2018) Petrogenesis and tectonic implications of the Late Triassic syenogranite in Qimantag area, East Kunlun Mountains. *Acta Petrologica et Mineralogica* 37(2):197–210 (in Chinese with English abstract)
- Zhao X, Fu LB, Wei JH, Bagas L, Santosh M, Liu Y, Zhang DH, Zhou HZ (2019) Late Permian back-arc extension of the eastern Paleo-Tethys Ocean: evidence from the East Kunlun Orogen, Northern Tibetan Plateau. *Lithos* 340–341:34–48
- Zhao X, Wei JH, Fu LB, Huizenga JM, Santosh M, Chen JJ, Wang DZ, Li AB (2020) Multi-stage crustal melting from Late Permian back-arc extension through Middle Triassic continental collision to Late Triassic post-collisional extension in the East Kunlun Orogen. *Lithos* 360:1–19

- Zheng Z, Chen YJ, Deng XH, Yue SW, Chen HJ, Wang QF (2018) Origin of the Bashierxi monzogranite, Qiman Tagh, East Kunlun Orogen, NW China: a magmatic response to the evolution of the Proto-Tethys Ocean. *Lithos* 296–299:181–194
- Zhou JH, Feng CY, Shen DL, Li DX, Wang H, Zhang MY, Ma SC (2015) Re-Os dating of molybdenite from the Yugouzi Fe-Cu(Mo) deposit in Qimantage, eastern Kunlun and its geological implications. *Geol Explor* 89(3):473–486 (in Chinese with English abstract)
- Zhou HZ, Zhang DH, Wei JH, Wang DZ, Santosh M, Shi WJ, Chen JJ, Zhao X (2020) Petrogenesis of Late Triassic mafic enclaves and host granodiorite in the Eastern Kunlun Orogenic Belt, China: implications for the reworking of juvenile crust by delamination-induced asthenosphere upwelling. *Gondwana Res* 84:52–70
- Zong KQ, Klemd R, Yuan Y, He ZY, Guo JL, Shi XL, Liu YS, Hu ZC, Zhang ZM (2017) The assembly of Rodinia: The correlation of early Neoproterozoic (ca.900 Ma) high-grade metamorphism and continental arc formation in the southern Beishan Orogen, southern Central Asian Orogenic Belt (CAOB). *Precambrian Res* 290:32–48

Springer Nature or its licensor holds exclusive rights to this article under a publishing agreement with the author(s) or other rightsholder(s); author self-archiving of the accepted manuscript version of this article is solely governed by the terms of such publishing agreement and applicable law.